日本磁気学会
ISSN 2432-0250
Journal of the Magnetics Society of Japan
Electronic Journal URL: https://www.jstage.jst.go.jp/browse/msjmag

Vol.47 No.2　2023

Journal

JOURNAL OF THE MAGNETICS SOCIETY OF JAPAN

Vol.47 No.2 2023

日本磁気学会

ISSN 2432-0250

HP: http://www.magnetics.jp/ e-mail: msj@bj.wakwak.com

Electronic Journal: http://www.jstage.jst.go.jp/browse/msjmag

世界初！
高温超電導型VSM

新製品

世界初*、高温超電導マグネットをVSMに採用することで
測定速度 当社従来機1/20を実現。
0.5mm cube磁石のBr, HcJ高精度測定が可能と
なりました。
*2014年7月 東英工業調べ

測定結果例

高温超電導VSMによるNdFeB(sint.) 0.5mm cube BHカーブ

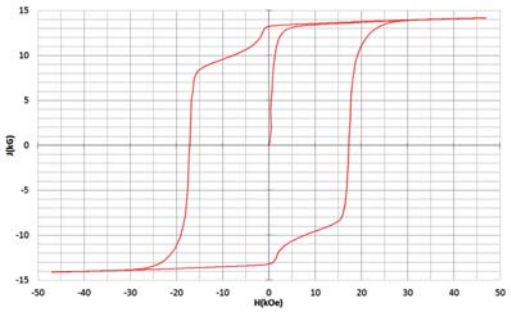

磁化測定レンジ：0.2emu
Br = 13.2kG　　HcJ = 17.2kOe

高温超電導VSMによるNdFeB(sint.) 1mm cube BHカーブ

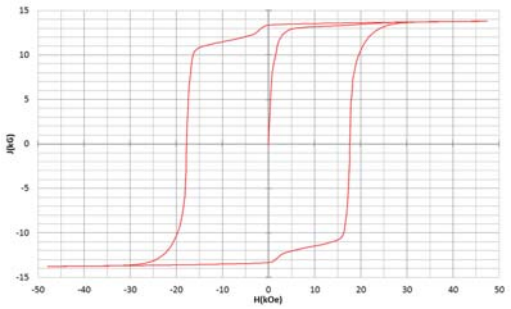

磁化測定レンジ：2emu
Br = 13.3kG　　HcJ = 17.7kOe

高温超電導VSMによるNdFeB(sint.) 4mm cube BHカーブ

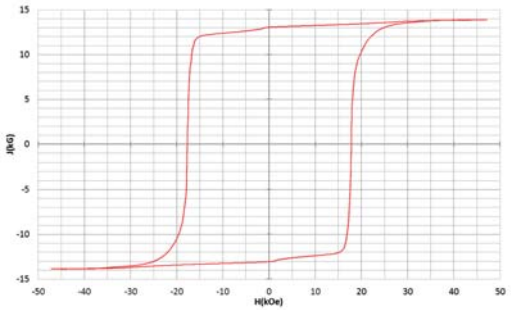

磁化測定レンジ：100emu
Br = 13.1kG　　HcJ = 17.8kOe

高速測定を実現

高温超電導マグネット採用により、高速測定を実現しました。Hmax= 5Tesla, Full Loop 測定が2分で可能です。
（当社従来機：Full Loop測定　40分）

小試料のBr,HcJ高精度測定

0.5mm cube 磁石のBr,HcJ高精度測定ができ、表面改質領域を切り出しBr,HcJの強度分布等、微小変化量の比較測定が可能です。
また、試料の加工劣化の比較測定が可能です。

試料温度可変測定

−50℃～+200℃温度可変UNIT（オプション）

磁界発生部の小型化

マグネットシステム部寸法：0.8m×0.3m×0.3m

TOEI 東英工業株式会社
http://www.toeikogyo.co.jp
〒194-0035 東京都町田市忠生1-8-13
TEL：042-791-1211 FAX：042-792-0490
E-mail : sales@toeikogyo.co.jp

Journal of the Magnetics Society of Japan
Vol. 47, No. 2

Electronic Journal URL: https://www.jstage.jst.go.jp/browse/msjmag

CONTENTS

J. Magn. Soc. Jpn., **47**, 28-37 (2023) <Review>

Research on spintronic functions of non-metallic materials and its modulation by external fields

M. Shiraishi

Department of Electronic Science and Engineendring, Kyoto University,
Kyoto-Daigaku-Katsura, Nishikyo-ku, Kyoto 615-8510, Japan.

Non-metallic materials, such as inorganic/organic semiconductors and topological quantum materials are now collecting significant attention in modern spintronics. The progress of the research field using the materials is quite rapid and tremendous amounts of significant studies have been published. In this review article, some important milestone works are introduced to enhance further acceleration of the research fields.

Key words: Organic semiconductors, graphene, inorganic semiconductors, silicon, topological insulator, Weyl ferromagnet, Weyl semimetal, spin injection, spin manipulation, gating effect

1. Introduction

Since the discovery of giant magnetoresistance effect, the field of spintronics has been rapidly expanding. As the first-generation material in spintronics, ferromagnetic and nonmagnetic metals have been and is still now playing the central role. Meanwhile, inorganic semiconductors have been collecting significant attention as the second-generation material in spintronics since the advent of diluted ferromagnetic semiconductor and spin transport in semiconductors. In the 21st century, novel materials systems such as organic molecules, hetero-interfaces, atomically flat materials and topological quantum materials are becoming rising stars of materials in spintronics. Attractiveness of non-metallic materials in spintronics is, for example, potential for spin modulation by external fields such as an electric field, long spin coherence and so on. In this review article, significant milestones in spintronics using such non-metallic materials including the author's achievements for the MSJ Award 2022 are introduced, albeit not all of the notable studies cannot be introduced because the field is rapidly expanding, and tremendous amounts of works have been implemented.

2. Spintronic function of molecular materials

Attractiveness of molecular materials in spintronics is its small spin-orbit interaction (SOI) attributed to its lightness, which allows expecting good spin coherence. Thus, molecular materials attracted much attention in the beginning of 21st century. In the advent of the research field, magnetoresistance in sexithienyl (T6) [1] and Alq3 [2] were reported by using a conventional electric two-terminal method, of which magnetoresistance (in Alq3) is shown in Fig. 1. Meanwhile, as widely recognized at present, superposition of anisotropic magnetoresistance in an electric local two-terminal method strongly hampers precise detection of spin transport signals, and sufficient elimination of spin-tunneling in molecules was not realized. Furthermore, long-term problems were missing of the Hanle-type spin precession and non-local four-terminal spin transport in most of works using molecules, where both achievements provide steadfast evidence of successful spin transport, albeit a trial to explain the missing was unsuccessfully implemented [3]. The problem also indicates the difficulty in estimating precise spin lifetime in molecules, and most of the works utilized a method of gap-dependence of spin signals instead of the Hanle method. However, to note is that the gap-dependence-like results can be obtained even in spin-dependent tunneling. Since most of molecular materials are low-conductive materials, identification of spin transport mechanisms, i.e., spin injection into molecules or spin-dependent tunneling via molecules, is difficult if spin transport in molecular materials would be successfully realized. Thus, the central research topics of the field with sufficient reliability is an interesting and unique physical feature of spin-dependent tunneling via molecules, where exotic

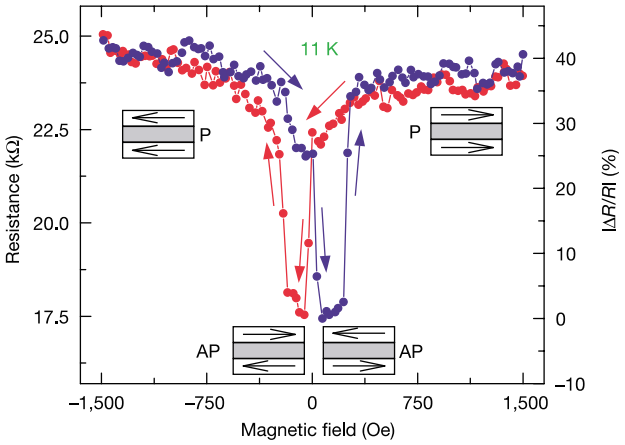

Fig. 1 Two-terminal magnetoresistance in a Co/Alq3/LaSrMnO spin valve (ref. 2)). Notable is an observation of negative magnetoresistance.

Corresponding author: M. Shiraishi
(e-mail: shiraishi.masashi.4w@kyoto-u.ac.jp).

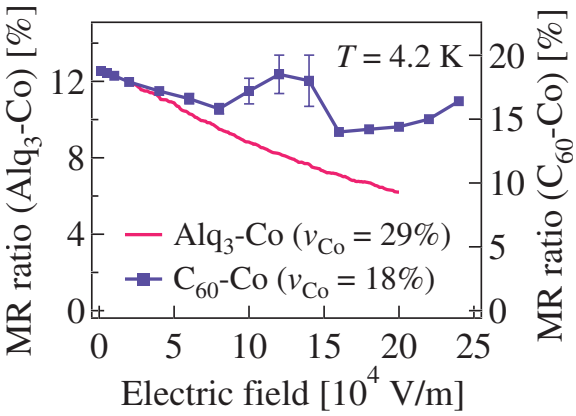

Fig. 2 Tunnel magnetoresistance in molecule-Co nanocomposite systems (ref. 5)).

enhancement of magnetoresistance ratio was discovered [4-7] (see Fig. 2), until the era of graphene spintronics. Although there were some contributions facing with the remaining serious problems in molecular spintronics [8], lack of serious devotion for solving these problems impedes further progress of the field, and at present, spintronics using molecules except for graphene is unfortunately shrinking. Novel approaches with showing reliable and reproducible evidence are still strongly awaited to help the field from severe stagnation.

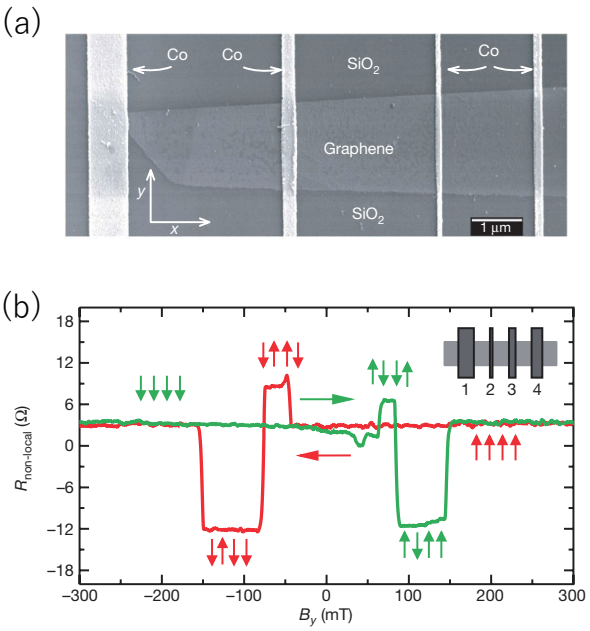

Fig. 3 Graphene spin valve (left) and observed non-local magnetoresistance at room temperature (right), where the non-local four-terminal measurement technique was introduced (ref. 11)).

Establishment of graphene spintronics strongly helps circumventing the serious stagnation of molecular spintronics. "Discovery" of single-layer graphene (SLG) exhibiting exotic and intriguing topological physics [9,10]

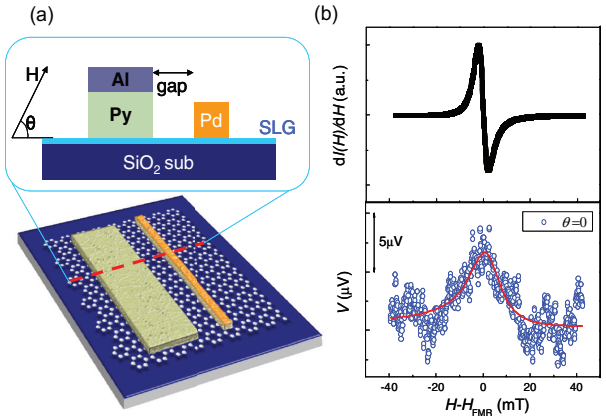

Fig. 4 (a) Spin transport device using single-layer graphene (SLG), where NiFe (Py) spin source and Pd spin current detector are equipped separately and an external magnetic field is applied to excite ferromagnetic resonance of the Py. (b) The upper panel shows the ferromagnetic resonance spectrum from the Py and the lower panel shows a concomitant electromotive force from the Pd. The external magnetic field is applied at θ =0. The resonance field is consistent with the field where the peak of the electromotive force appears, which is an evidence of successful spin injection and transport in SLG by spin pumping (ref. 15)).

provided great impact in broad research fields. Quite small effective mass of electrons and holes in SLG enables quite fast charge motion with high mobility and lightness of SLG consisting of only carbon atoms allows good spin coherence, both of which are appropriate physical nature for spin transport. Since 2007, the field of graphene spintronics rapidly expanded, where realization of room temperature spin transport[11,12] by the non-local four-terminal method (Fig. 3), spin lifetime anisotropy/isotropy [13,14], and so forth, and now spin relaxation physics of not only SLG but also bilayer graphene is investigated and understood in detail.

It is also quite notable that graphene spintronics explored an avenue towards van der Waals heterostructure spintronics, where bilayer of SLG and transition metal dichalcogenides (TMDs) is collecting broad attention in view of proximity effect of the SOI.

Notable experimental methods applicable to spin transport measurements for molecular materials are dynamical spin injection. A pioneering work was carried out by using CVD-grown graphene, where room temperature spin transport in SLG was demonstrated in a lateral spin device with separated spin source and detector electrodes (see Fig. 4) [15]. A subsequent achievement of dynamical spin injection into molecule was achieved as polaron spin current transport in conjugated polymer [16] by introducing a vertical spin device for dynamical spin injection and detection in condensed matters [17]. As in semiconductor spintronics, it is corroborated that dynamical spin injection can be a

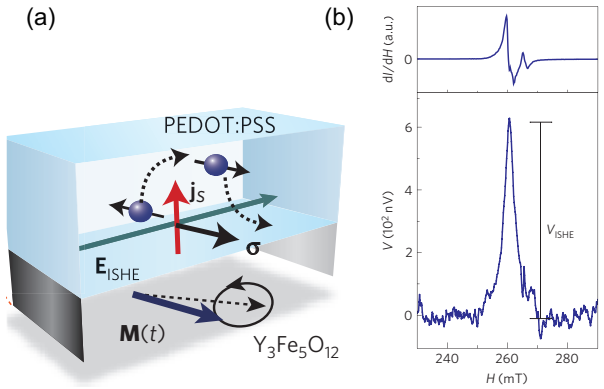

Fig. 5 (a) Device structure of organic spin convertor. Organic polymer, PEDOT:PSS, is equipped on ferrimagnetic insulator, $Y_3Fe_5O_{12}$ (YIG). (b) The upper panel shows the ferromagnetic resonance spectrum from the YIG and the lower panel shows a concomitant electromotive force from the organic polymer. Again, the magnetic fields where the ferromagnetic resonance and the electromotive force peaks appear are consistent (ref. 18)).

potential approach for injecting spins into molecules. The other notable achievement based on the dynamical spin pumping technique in molecular spintronics is demonstration of spin conversion. As aforementioned, a characteristic nature of molecular materials in spintronics is its weak SOI. Hence, people had been believing that spin charge conversion is impossible in molecules because its SOI is too weak to realize the conversion. The achievement by Ando et al. overturned the conventional understanding (see Fig. 5) [18]. The key for the successful spin conversion in molecules is sufficient spin accumulation by the spin pumping from YIG as the substrate of PEDOT:PSS, a solution-processed spin convertor. Although the conversion efficiency was indeed small, the sufficient spin accumulation into the polymer allows detection of charge flow generated by the inverse spin Hall effect (ISHE). This work opened a new frontier of spin conversion physics, where heavy elements and topological materials played pivotal roles. The same concept was applied for substantiating spin conversion in SLG [19-21], where there was strong debate regarding the mechanisms. The sample structure was the same, SLG/YIG bilayer, in the studies. Mendez et al. claimed that the spin conversion was governed by the Rashba-Edelstein effect due to inversion symmetry breaking along the perpendicular to the SLG plane direction [20]. Meanwhile, our group reported that the ISHE governs the conversion physics by demonstrating ambipolar and gate-modulated spin conversion (see Fig. 6) [21]. The conclusive work was implemented by Raes et al. [14], where spin relaxation in SLG is isotropic resulting in no Rashba field is created in SLG instead of its inversion symmetry breaking along the perpendicular to the plane direction, which unequivocally negated the claim by Mendez et al.

In summary, progress of molecular spintronics is still

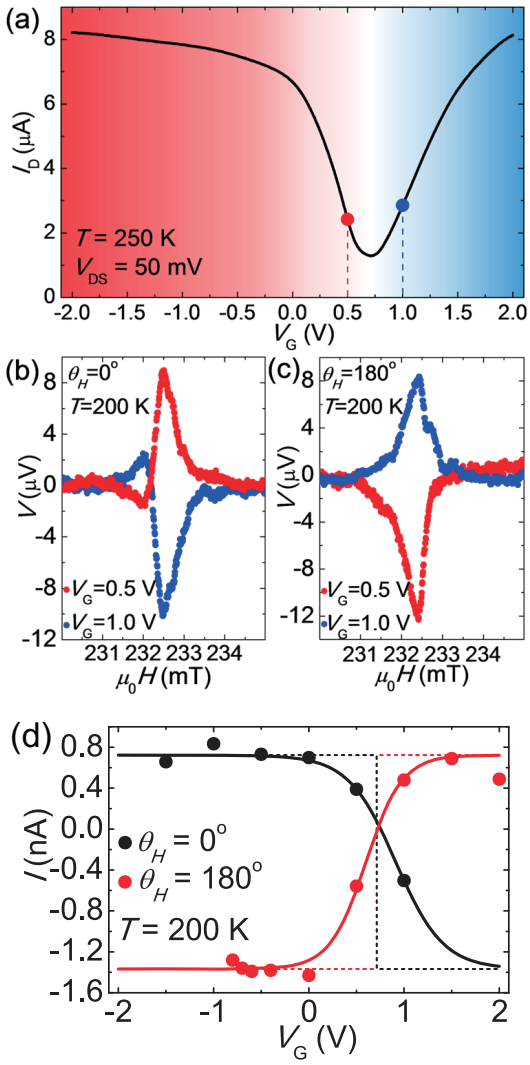

Fig. 6 (a) Gate voltage dependence of the source-drain electric current in SLG. (b) Gate voltage dependence of electromotive forces in SLG under spin pumping when the carrier is hole (+0.5 V, the red solid line) and electron (+1.0 V, the blue solid line). (c) Gate voltage dependence of the electromotive forces in SLG when the direction of the external magnetic field is reversed. (d) Gate voltage dependence of generated electric current by the ISHE. The saturation of the current under higher gate voltages is compelling evidence that the ISHE, not the Rashba-Edelstein effect, governs the spin conversion (ref. 21)).

lagged of the other spintronics fields and its attractiveness has not been explored yet. Hence, much serious effort is awaited.

3. Spintronic function of topological quantum materials

A topological quantum material (TQM) is a novel material phase in 21st century. Since the discovery of the new material phase [22-24], tremendous effort has been made to explore a wide variety of novel and abundant physics appearing in topological insulators (TIs),

topological superconductors (TSCs), Weyl semimetals and Weyl ferromagnets for creating novel electric and spintronics devices by utilizing their fast carrier mobilities due to the linear band structures. Contrary to topologically trivial materials, TQMs exhibit great potential to show exotic and intriguing physical properties. TIs possess spin-polarized Dirac fermion bands resulting in the quantum spin Hall effect and persistent spin current that are resilient to defects [25], and TSCs can be a material platform for realizing fault-tolerant quantum computing utilizing Majorana fermions that can exist in TSC states [26]. A Weyl semimetal is a considerably new family of TQMs [27], where nondegenerate linear conduction and valence bands touch each other at the Weyl point by breaking either spatial or time reversal symmetries, yielding gapless Weyl fermions. In addition, a Weyl semimetal is known to be an ideal material platform of the appearance of the Adler-Bell-Jackiw (ABJ) anomaly of Weyl fermions [28], which is due to the breaking of chiral symmetry in massless Weyl fermions under quantum fluctuation. The ABJ anomaly was experimentally corroborated in TaAs, NbAs, TaP and WTe_2 [29-32] and is the fingerprint of the Weyl nature. A Weyl ferromagnet and anti-ferromagnet are also a novel family of TQMs, where Co_2MnGa [33] and Mn_3Sn [34] are representative materials, respectively, and a number of spin-related effects, such as giant anomalous Hall [35,36] and Nernst effects [35], giant spin-Hall and inverse spin-Hall effects [37] in Co_2MnGa and the magnetic spin Hall effect (a novel family of Hall effects) [38] in Mn_3Sn, has been discovered and detected. Because tremendous amounts of works have been implemented, it is difficult to cover and follow the whole research topics for TQMs, the author introduces his own and related works regarding spin polarization detection in this chapter.

As aforementioned, topologically-protected surface spin polarization in TIs is an intriguing research object in spintronics, and much effort was paid for detecting the spin polarization. Two possible pathways to the goal; a potentiometric method and a spin pumping method. The first study to claim the detection of the surface spin polarization was implemented by using Bi_2Se_3, a three-dimensional TI [39], where the potentiometric method was utilized. However, strong debate arose about what the authors detected, because the Fermi level of Bi_2Se_3 is located in the conduction band and the topological state is buried into the topologically trivial bulk state. Thus, a question that the authors detected spin polarization attributed not to the topological state but to the Rashba state. The similar debate also arose to the claim of the room temperature detection of the topological surface state in Bi_2Se_3. To avoid such confusion, identification of the polarity of the spin signals, which comes from the spin alignments of the surface spin current of a TI and detector ferromagnet, is quite significant [40], and control experiments to support a claim is indispensable. Thus, comparison of results in a bulk non-insulative TI (such as

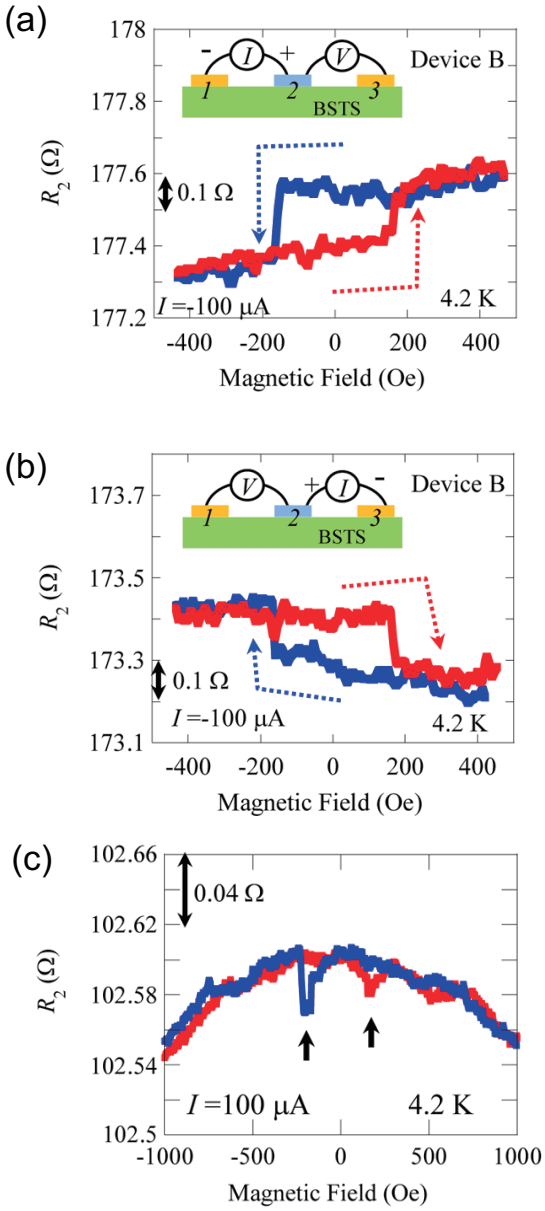

Fig. 7 (a) Magnetoresistance due to the topologically-protected surface spin polarization in BiSbTeSe at 4.2 K. (b) Magnetoresistance in BiSbTeSe when the direction of the charge flow was reversed. Polarity of the magnetoresistance was opposite to that in (a). (c) Missing magnetoresistance in BiSe at 4.2 K, which signifies the position of the Fermi level is crucial for successful detection of the surface spin polarization in topological insulator (ref. 41)).

Bi_2Se_3) and a bulk insulative TI (such as $Bi_{1.5}Sb_{0.5}Te_{1.7}Se_{0.3}$) is quite important. Indeed, the authors' group introduced $Bi_{1.5}Sb_{0.5}Te_{1.7}Se_{0.3}$ as a possible candidate TI and reported successful detection of the surface spin polarization up to ca. 150 K (Fig. 7) [41]. The spin signal is detectable only from $Bi_{1.5}Sb_{0.5}Te_{1.7}Se_{0.3}$ and no signal is observed in Bi_2Se_3 even at 4 K, which is compelling evidence that the detected spin signal is

ascribed to the topologically-protected surface helical spin state. To note is that the similar comparison was carried out in the spin pumping approach [42].

Topological nature in TQMs allows the other intriguing physics in Weyl materials. TaAs is the first material as a Weyl material [43], and a Weyl material collects significant attention because of its band-crossing points that give rise to plenty of unique physical properties, such as the Fermi arc surface states, the chiral anomaly coming from the Nielsen-Ninomiya theorem [44] and monopole-like Berry curvature [45]. In addition, a prominent class of Weyl semimetals is Weyl magnetic materials such as ferromagnetic Co_2MnGa and antiferromagnetic Mn_3Sn. These two materials are playing pivotal roles in condensed-matter physics because of the recent discoveries of the gigantic anomalous Hall effect (AHE) [46,47], the magnetic spin Hall effect (a novel family of Hall effects) [48], and spin caloritronics phenomena such as the large anomalous Nernst effect [49,50]. Additionally, magnetic Heusler alloys have emerged as promising materials in the field of spintronics due to their either half-metallic or semimetallic nature, which would lead to a high spin polarization [51,52], as has been reported in Co-based full Heusler compounds [53,54]. Co_2MnGa is a representative Weyl ferromagnet as aforementioned, and sizable spin Hall effect (SHE) and ISHE can be expected due to its topological nature like in the case of AHE. Indeed, coexistence of the giant ISHE and the SHE was corroborated by using the electric non-local four-terminal method [55] and more importantly, it was observed that Onsager's reciprocity does not hold for the system unlike for conventional metallic ferromagnets (see Fig. 8) [56]. Furthermore, two orders of magnitude enhancement of magnetoresistance attributed to the anomalous Nernst effect in single Co_2MnGa wire was also reported [57].

Not only Weyl ferromagnets and antiferromagnets, but a Weyl semimetal also enable significant spintronic effects. Among a number of Weyl semimetals, the T_d-type WTe_2 [58] possesses abundant spintronic nature, where the Weyl points appear at the crossing of the oblique conduction and valence bands due to the broken inversion symmetry and nonsaturating giant positive magnetoresistance is a manifestation of the type-II Weyl character [59,60]. As aforementioned, fictitious magnetic monopoles can appear at each Weyl point, which gives rise to in-plane spin polarization at the surface of the Weyl semimetal [61,62]. In fact, the in-plane spin polarization along the *b*-axis (S_y, parallel to the WTe_2 plane) is ascribed to the Weyl node, which was electrically detected [63]. Meanwhile, the S_y polarization disappears at very low temperature (< 15 K) due to lattice expansion, which has been hampering spin information propagation and extraction at higher temperature available for all-electric spin devices. Importantly, angle-resolved photoemission spectroscopy (ARPES) revealed other possible spin polarizations along the *c*-axis (S_z, perpendicular to the plane) in addition to those along the *b*-axis in WTe_2 [64]. A pioneering work utilizing the S_z polarization of WTe_2 is detection of anomalous spin torque in ST-FMR (see Fig. 9) [65,66]. The authors introduced a potentiometric approach to create and detect the S_z polarization, and experimentally proved that the S_z polarization is quite resilient to thermal

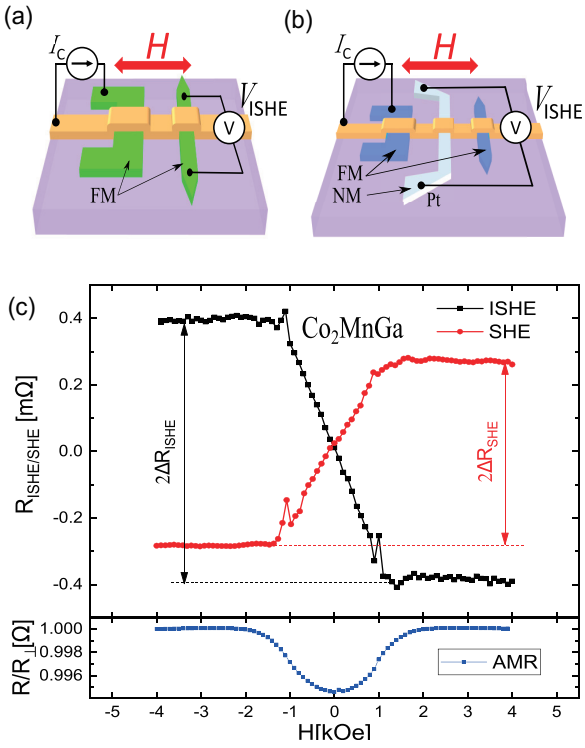

Fig. 8 Measuring setups for the ISHE (a) and the SHE (b) in Co_2MnGa, a Weyl ferromagnet. (c) Spin resistances due to the ISHE and the SHE, where Onsager reciprocity is broken (ref. 55)).

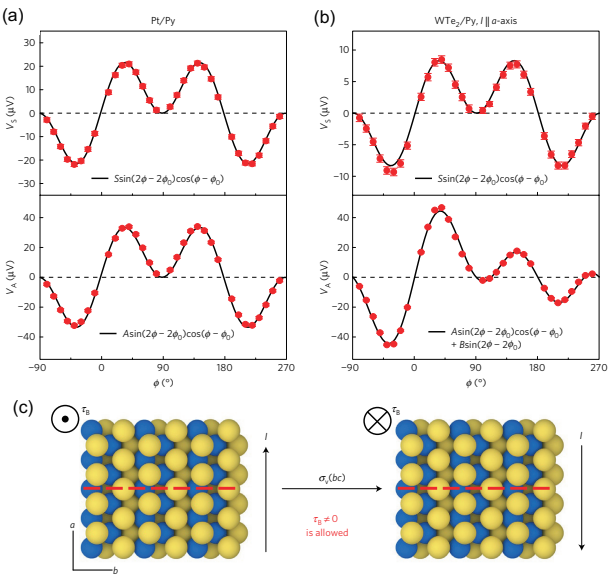

Fig. 9 Anomalous spin-orbit torque (SOT) appearing in T_d-type WTe_2. (a) SOT in Pt/Py and (b) SOT in WTe_2/Py, where the electric current flows along the *a*-axis. (c) Schematic images of structural symmetry breaking in WTe_2 (ref. 65)).

fluctuation and spin signals are detectable up to RT [67], which enables creation of all-electric spin devices using a Weyl semimetal (Fig. 10).

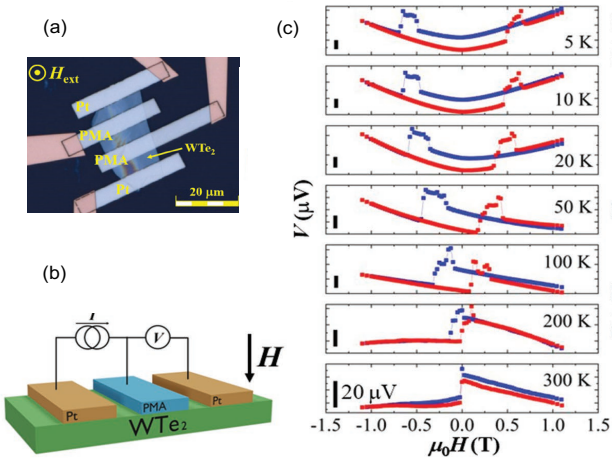

Fig. 10 (a) Optical microscopic view of an all-electric spin device using T_d-type WTe_2, a Weyl semimetal. (b) Measuring setup for the S_z spin polarization detection created in the WTe_2. (c) Temperature dependence of magnetoresistance of the WTe_2 spin device. The S_z spin polarization is attributed to structural symmetry breaking along the *b*-axis in WTe_2 and is resilient to thermal fluctuation (ref. 67)).

In summary, horizon of topological spintronics is expanding rapidly, and a number of experimental approaches allows investigating significant and attractive topological nature in TQMs in spintronic viewpoints.

4. Spintronic function of inorganic semiconductors

For several decades, inorganic semiconductors play one of central roles in material choice in spintronics. There are two pivotal trends in inorganic semiconductor spintronics: (1) diluted magnetic semiconductors, and (2) spin transport in semiconductors. Regarding the first topic, epoch-making achievements, such as electric-field control of ferromagnetism in InMnAs [68] and realization of RT ferromagnetism in InFeAs [69] since the first realization of diluted magnetic semiconductor [70]. Meanwhile, unfortunately, the author has not been focusing his work on the material, and in this chapter, the author sheds light only on spin transport in inorganic semiconductor, especially group-IV inorganic semiconductors.

Spin injection, transport, detection and manipulation in inorganic semiconductor are key scientific issues for applications towards spin-based transistors. In principle, two different types of spin transistors using inorganic semiconductors are: (1) Das-Datta type [71] and (2) Sugahara-Tanaka type [72]. In addition, the Sugahara-Tanaka type spin transistor allows a new spin logic system, the Dery-Sham type spin logic [73]. To note is that compound inorganic semiconductors such as III-V

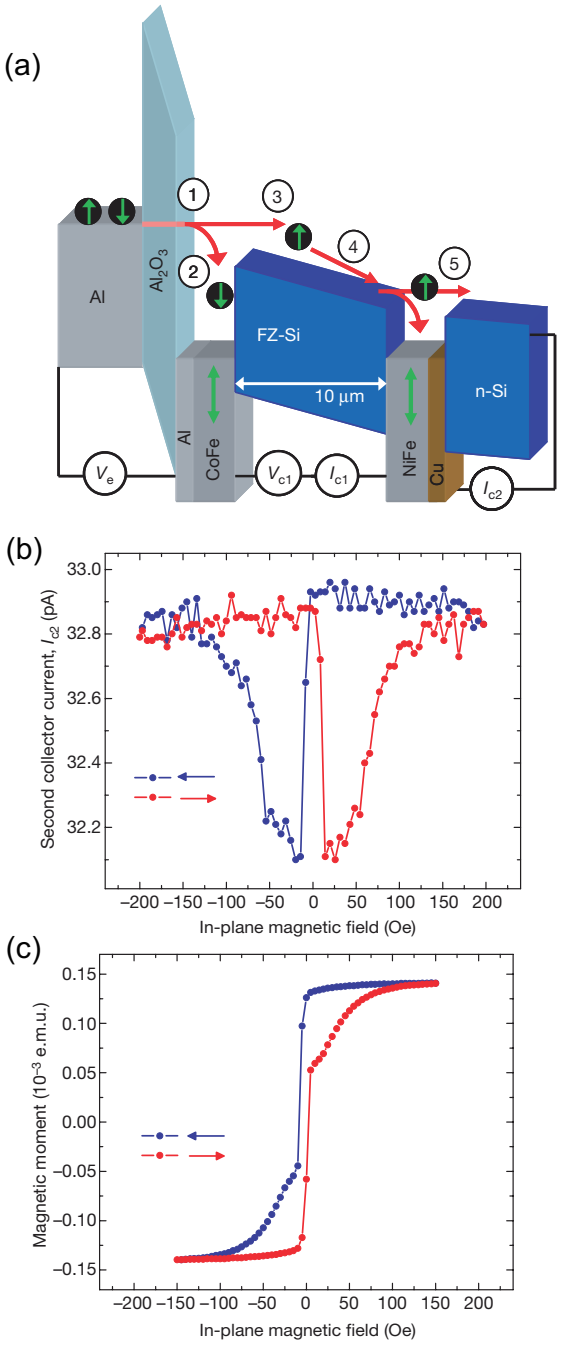

Fig. 11 (a) Schematic image of Si-based hot-electron transistor. (b) Magnetoresistance effect due to spin injection and spin transport via 10 mm non-doped Si. (c) Magnetization curves of the CoFe electrode (ref. 74)).

semiconductors are available to the Das-Datta type and group IV inorganic semiconductors including graphene are suitable for the Sugahara-Tanaka type, since operation principles of both transistors are different. Group-IV semiconductors (diamond, Si and Ge) possess lattice inversion symmetry and carbon and Si are light elements, which is the underlying physics of possible long spin coherence in the materials, such as graphene and Si, and is the reason why these materials garner much

attention. In fact, graphene exhibits long-range spin transport over 10 mm, whereas spin lifetime in graphene is merely about tens picoseconds mainly due to its large Fermi velocity originating from the Dirac nature of graphene. Si exhibits long spin lifetime over several nanoseconds and relatively long spin diffusion length of over 1 mm, i.e., long spin lifetime and diffusion length successfully coexist.

The chronicle of Si spintronics substantially started from hot-electron spin injection into non-doped Si (Fig. 11) [74], although some challenging but unsuccessful works using some different approaches had been reported before. The authors of ref. 74 introduced a hot-electron transistor structure, where the wafer bonding technique was used, and realized spin injection up to 260 K [75], long-range spin transport of 2 mm [76], and multiple spin precession of 13p due to the Hanle effect [77]. The notable is that this approach elaborately circumvents the reliability problem of the electric two-terminal method as partly described in Chap. 2. These achievements manifested great spintronic potential of Si and greatly stimulated researchers in semiconductor spintronics. Meanwhile, since the hot-electron transistor structure was used, the output spin signal was considerably small to be an order of picoampere and modulation of spin signal by gating was difficult, which can strongly hinder practical application of Si-based spin devices. Thus, reliable and reproducibly spin injection and transport in Si by the other approach available for spin transistors. The authors introduced the electric non-local four-terminal method to achieve successful spin injection and creation of pure spin current in Si [78], and room temperature spin injection/transport/detection in n-type degenerate Si with Hanle-type spin precession was achieved (see Fig. 12) [79]. Furthermore, spin injection/transport/detection in non-degenerate n-type Si and subsequent spin signal modulation by gating were achieved at room temperature [80,81], where the on/off ratio was enhanced >10^4 (Fig. 13) [81]. In the course of these significant studies, a number of detailed spintronic physics in Si were clarified: spin drift in Si [82,83], bias voltage dependence of spin signals [84], clarification of the origin the "inverted Hanle" effect [85], enhancement of spin signals by utilizing spin drift and clarification of its underlying physics [86-88], achievement of thermal spin injection in Si [89], investigation of gating effects on spin signals [90], and thermal annealing effects on spin signals [91,92]. Notable achievements in Si spintronics from application-oriented viewpoints are

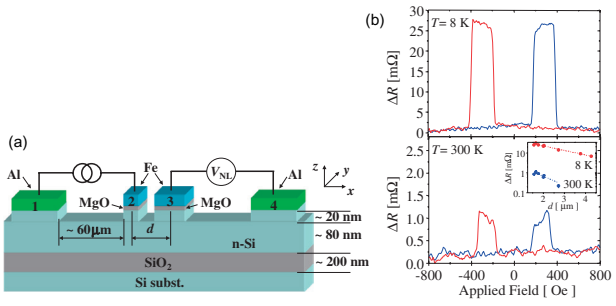

Fig. 12 (a) Schematic image of a four-terminal degenerate n-type Si spin valve. (b) Non-local magnetoresistance in the Si spin valve at 8 K (the upper panel) and 300 K (the lower panel). The inset of the lower panel shows gap-length dependence of spin resistances (ref. 79)).

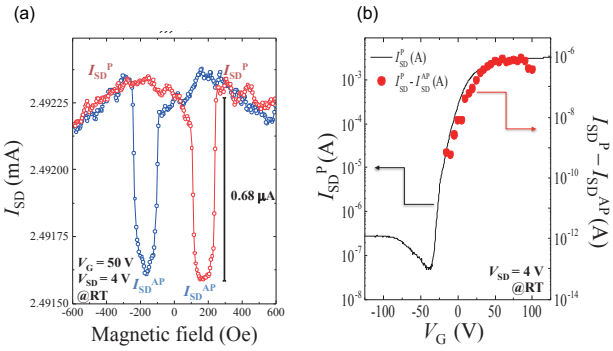

Fig. 13 (a) Magnetoresistance in spin-dependent electric current of non-degenerate n-type spin MOSFET at room temperature. (b) Gate voltage dependence of the source-drain current (the black solid line) and spin signals (the red closed circles) (ref. 81)).

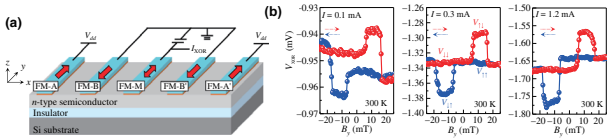

Fig. 14 (a) Spin logic circuit made of Si spin MOSFET. (b) An example XOR logic operation of the Si spin logic. For detail, see ref. 94).

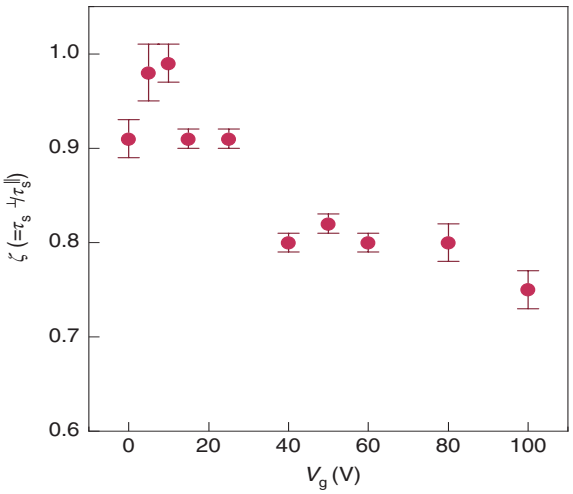

Fig. 15 Spin lifetime anisotropy in in-plane and perpendicular-to-the-plane spins in Si spin MOSFET as a function of gate voltages. The anisotropy exists without a gate voltage due to the built-in Rashba field in the Si channel, and the anisotropy is once suppressed by the gate voltage application (ref. 96)).

demonstration of over 1% magnetoresistance ratio [93] and spin logic operation (Fig. 14) [94]. Furthermore, significant achievements in basic physics viewpoints are spin-pumping-induced spin transport in p-type Si [95] and electric field modulation of spin precession (spin manipulation without an external magnetic field) due to synthetic Rashba field in Si/SiO_2 [96]. Especially, spin manipulation by the gate electric field in Si spin FET shown in Fig. 15 counters conventional understandings that the SOI in Si is negligibly small and the Rashba field does not play a dominant role in Si. The achievement can be regarded as one of subsequent studies that gate control of SOI, resulting in the ISHE, in ultrathin metallic films [97-99]. It is also noted that spin transport in the other group-IV semiconductor, Ge, was also achieved at room temperature by spin pumping [100], which enables subsequent studies using Ge towards spin transistor creation [101,102].

In summary, inorganic semiconductors are playing one of pivotal roles in spintronics, and its research field expands to both application-oriented and fundamental directions. Especially, group-IV semiconductors such as Si and Ge (and in addition, graphene and diamond) play an important role in the field.

Acknowledgements The author is indebted to all collaborators, especially Prof. Yoshishige Suzuki and his group members in Osaka University, and Dr. Tomoyuki Sasaki, Mr. Hayato Koike and group members in TDK corporation. He also acknowledges to his colleagues and students of his group in Osaka University (2010-2013) and Kyoto University (2013-) especially Dr. Eiji Shikoh, Dr. Yuichiro Ando, Dr. Ryo Ohshima, Dr. Ei Shigematsu and Dr. Eiiti Tamura, for their strong and supportive collaboration. Financial supports from the Ministry of Education, Culture, Sports, Science and Technology of Japan and the Japan Science and Technology Agency are deeply appreciated.

References

1) V.A. Dediu, M. Murgia, F.C. Matacotta, C. Taliani and S. Barbaner: *Solid State Commun.* **122**, 181 (2002).
2) Z. Xiong, D. Wu, Z. Valy Vardeny and J. Shi: *Nature* **427**, 821 (2004).
3) P.A. Bobbert, W. Wagemans, F.W.A. van Oost, B. Koopmans and M. Wohlgenannt: *Phys. Rev. Lett.* **102**, 156604 (2009).
4) S. Miwa, M. Shiraishi, M. Mizuguchi, T. Shinjo and Y. Suzuki: *Jpn. J. Appl. Phys.* **45**, L717 (2006).
5) S. Miwa, M. Shiraishi, S. Tanabe, M. Mizuguchi, T. Shinjo and M. Shiraishi: *Phys. Rev. B***76**, 214414 (2007).
6) D. Hatanaka, S. Tanabe, H. Kusai, R. Nouchi, T. Nozaki, T. Shinjo, Y. Suzuki, H. Wan, K. Takanashi and M. Shiraishi: *Phys. Rev. B***79**, 235402 (2009).
7) Y. Sakai, E. Tamura, S. Toyokawa, E. Shikoh, V.K. Lazarov, A. Hirohata, T. Shinjo, Y. Suzuki and M. Shiraishi: *Adv. Func. Mater.* **22**, 3845 (2012).
8) "A better spin on organic semiconductors" (editorials): *Nature Nanotech.* **8**, 611 (2013).
9) K.S. Novoselov, A.K. Geim, S.V. Morozov, D. Jiang, M.I. Latsnelson, I.V. Grigorieva, S.V. Dubonos and A.A. Firsov: *Nature* **438**, 197 (2005).
10) Y. Zhang, Y-W. Tan, H.L. Stormer and P. Kim: *Nature* **438**, 201 (2005).
11) N. Tombros, C. Jozsa, M. Popinciuc, H.T. Jonkman and B.J. van Wees: *Nature* **448**, 571 (2007).
12) M. Ohishi, M. Shiraishi, R. Nouchi, T. Nozaki, T. Shinjo and Y. Suzuki: *Jpn. J. Appl. Phys.* **46**, L605 (2007).
13) N. Tombros, S. Tanabe, A. Veligura, C. Jozsa, M. Popinciuc, H.T. Jonkman and B.J. van Wees: *Phys. Rev. Lett.* **101**, 046601 (2008).
14) B. Raes, J.E. Scheerder, M.V. Costache, F. Bonell, J.F. Sierra, J. Cuppens, J. Van de Vondel and S.O. Valenzuela: *Nature Commun.* **7**, 11444 (016).
15) Z. Tang, E. Shikoh, H. Ago, K. Kawahara, Y. Ando, T. Shinjo and M. Shiraishi: *Phys. Rev. B***87**, 140401(R) (2013).
16) S. Watanabe, K. Ando, K. Kang, S. Mooser, Y. Vaynzof, H. Kurebayashi, E. Saitoh and H. Sirringhaus: *Nature Phys.* **10**, 308 (2014).
17) Y. Kitamura, E. Shikoh, Y. Ando, T. Shinjo and M. Shiraishi: *Sci. Reports* **3**, 1739 (2012).
18) K. Ando, S. Watanabe, S. Mooser, E. Saitoh and H. Sirringhaus: *Nature Mater.* **12**, 622 (2013).
19) R. Ohshima, A. Sakai, Y. Ando, T. Shinjo, K. Kawahara, H. Ago and M. Shiraishi: *Appl. Phys. Lett.* **105**, 162401 (2014).
20) J.B.S. Mendes, O. Alves Santos, L.M. Mireles, R.G. Lacerda, L.H. Viela-leao, F.L.A. Machado, R.L. Rodriguez-Suarez, A. Azevedo and S.M. Rezende: *Phys. Rev. Lett.* **115**, 226601 (2015).
21) S. Dushenko, H. Ago, K. Kawahara, T. Tsuda, S. Kuwabata, T. Takenobu, T. Shinjo, Y. Ando and M. Shiraishi: *Phys. Rev. Lett.* **116**, 166102 (2016).
22) M.Z. Hasan and C.L. Kane: *Rev. Mod. Phys.* **82**, 3045-3067 (2010).
23) Z.-L. Qi and S.-C. Zhang: *Rev. Mod. Phys.* **83**, 1057-1110 (2011).
24) N.P. Armitage, E.J. Mele and A. Vishwanath: *Rev. Mod. Phys.* **90**, 015001 (2018).
25) C.L. Kane and E.J. Mele: *Phys. Rev. Lett.* **95**, 226801 (2005).
26) M. Sato and S. Fujimoto: *J. Phys. Soc.* Jpn. **85**, 072001 (2016).
27) S. Murakami: *New J. Phys.* **9**, 356 (2007).
28) H.B. Nielsen and M. Ninoymiya: *Phys. Lett. B***130**, 389 (1983).
29) C.-L. Zhang et al.: *Nat. Commun.* **7**, 10735 (2016).
30) X.C. Huang et al.: *Phys. Rev. X* **5**, 031023 (2015).
31) F. Arnold et al.: *Nat. Commun.* **7**, 11615 (2016).
32) Y-Y. Lv et al.: *Phys. Rev. Lett.* **118**, 096603 (2017).
33) I. Belopolski, K. Manna, D.S. Sanchez, G. Chang, B. Ernst, J. Yin, S.S. Zhang, Y. Cochran, N. Shumiya, M. Z. Hasan: *Science* **365**, 1278 (2019).
34) K. Kuroda, T. Tomita, M.-T. Suzuki, C. Bareille, A. A. Nugroho, P. Goswami, M. Ochi, M. Ikhlas, M. Nakayama, S. Akebi, R. Noguchi, R. Ishii, N. Inami, K. Ono, K. Kumigashira, A. Varykhalov, T. Muro, T. Koretsune, R. Arita, S. Shin, Takeshi Kondo, and S. Nakatsuji: *Nature Mater.* **16**, 1090 (2017).
35) A. Sakai, Y. P. Mizuta, A. A. Nugroho, R. Sihombing, T. Koretsune, M.-T. Suzuki, N. Takemori, R. Ishii, D. Nishio-Hamane, R. Arita, P. Goswami, and S. Nakatsuji: *Nature Phys.* **14**, 1119 (2018).
36) G. Chang, S. Y. Xu, X. Zhou, S. M. Huang, B. Singh, B. Wang, I. Belopolski, J. Yin, S. Zhang, A. Bansil, H. Lin, and M. Z. Hasan: *Phys. Rev. Lett.* **119**, 156401 (2017).
37) L. Leiva, S. Granville, Y. Zhang, S. Dushenko, E. Shigematsu, T. Shinjo, R. Ohshima, Y. Ando and M. Shiraishi: *Phys. Rev. B***103**, L041114 (2021).
38) M. Kimata, H. Chen, K. Kondou, S. Sugimoto, P. K. Muduli, M. Ikhlas, Y. Omori, T. Tomita, A. H. MacDonald, S. Nakatsuji, and Y. Otani: *Nature* **565**, 627 (2019).
39) C. Li, O.M. van't Erve, J.T. Robinson, Y. Liu, L. Li, B.T.

Jonker: *Nat. Nanotech.* **9**, 218 (2014).
40) E.K. de Vries, A.M. Kamerbeck, N. Koirala, M. Brahlek, M. Salehi, S. Oh, B.J. van Wees and T. Banerjee: *Phys. Rev. B***92**, 201102(R) (2015).
41) Yu. Ando, T. Hamasaki, T. Kurokawa, K. Ichiba, F. Yang, M. Noval, S. Sasaki, K. Segawa, Yo. Ando and M. Shiraishi: *Nano Lett.* **14**, 6226 (2014).
42) Y. Shiomi, K. Nomura, Y. Kajiwara, K. Eto, M. Novak, K. Segawa, Yo. Ando and E. Saitoh: *Phys. Rev. Lett.* **113**, 196601 (2014).
43) B.Q. Lv et al.: *Phys. Rev. X* **5**, 031013 (2015).
44) H. Nielsen and M. Ninomiya, Phys. Lett. B **130**, 389 (1983).
45) H. Yang, Y. Sun, Y. Zhang, W.-J.Shi, S.S. Parkin and B. Yan: *New J. Phys.* **19**, 015008 (2017).
46) A. Sakai et al.: *Nature Phys.* **14**, 1119 (2018).
47) G. Chang et al.: *Phys. Rev. Lett.* **119**, 156401 (2017).
48) M. Matsuda, N. Kanda, T. Higo, N. Armitage, S. Nakatsuji and R. Matsunaga: *Nature Commun.* **11**, 909 (2020).
49) B.M. Ludbrook, B.J. Ruch and S. Granville: *Appl. Phys. Lett.* **110** 062408 (2017).
50) S. Kanatsuji, N. Kiyohara and T. Higo: *Nature* **527**, 212 (2015).
51) H. Reichlova et al.: *Appl. Phys. Lett.* **113**, 212405 (2018).
52) J.M.D. Coery and M. Venkatesam: *J. Appl. Phys.* **91**, 8345 (2002).
53) C. Felser and G.H. Hecher: *Spintronics: From Materials to Devices* (Springer, Dordrecht, Heidelberg, New York, London, 2013).
54) T. Kimura, N. Hashimoto, S. Yamada, M. Miyao and K. Hamaya: *NPG Asia Mater.* **4**, e9 (2012).
55) L. Leiva, S. Granville, Y. Zhang, S. Dushenko, E. Shigematsu, T. Shinjo, R. Ohshima, Y. Ando and M. Shiraishi: *Phys. Rev. B***103**, L041114 (2021).
56) Y. Omori, E. Sagasta, Y. Niimi, M. Gradhand, L.E. Hueso, F. Casanova and Y. Otani: *Phys. Rev. B***99**, 014403 (2019).
57) L. Leiva, S. Granville, Y. Zhang, S. Dushenko, E. Shigematsu, T. Shinjo, R. Ohshima, Y. Ando and M. Shiraishi: *Phys. Rev. Materials* **6**, 064201 (2022).
58) A.A. Soluyanov, D. Gresch, Z. Wang, Q. Wu, M. Troyer, X. Dai, B.A. Bernevig: *Nature* **527**, 495 (2015).
59) M.N. Ali, J. Xiong, S. Flynn, J. Tao, Q.D. Gibson, L.M. Schoop, T. Liang, N. Haldolaarachchige, M. Hirschberger, N.P. Ong, R.J. Cava: *Nature* 514, 205 (2014).
60) Y. Qi et al.: *Nat. Commun.* **7**, 11038 (2015).
61) H.B. Nielsen, M. Ninomiya: *Nucl. Phys. B* **185**, 20 (1981).
62) H.B. Nielsen, M. Ninomiya: *Nucl. Phys. B* **193**, 173 (1981).
63) P. Li, W. Wu, Y. Wen, C. Zhang, J. Zhang, S. Zhang, Z.Yu, S.A. Yang, A. Manchon, X-x. Zhang: *Nat. Commun.* **9**, 3990 (2018).
64) P.K. Das, D.D. Sante, I. Vobornk, J. Fujii, T. Okuda, E. Bruyer, A. Gyenis, B.E. Feldman, J. Tao, R. Ciancio, G. Rossi, M.N. Ali, S. Picozzi, A. Yazdani, G. Panaccione, R.J. Cava: *Nat. Commun.* **7**, 10847 (2016).
65) D. MacNeil, G.M. Stiehl, M.H.D. Guimaraes, R.A. Buhrman, J. Park, D.C. Ralph: *Nat. Phys.* **13**, 300 (2017).
66) D. MacNeil, G.M. Stiehl, M.H.D. Guimaraes, N.D. Reynolds, R.A. Buhrman, D.C. Ralph: *Phys. Rev. B* **96**, 054450 (2017).
67) K. Ohnishi, M. Aoki, R. Ohshima, E. Shigematsu, Y. Ando, T. Takenobu and M. Shiraishi: *Adv. Electron. Mater.* **8**, 2200647 (2022).
68) H. Ohno, D. Chiba, F. Matsukura, T. Omiya, E. Abe, T. Dietl, Y. Ohno and K. Ohtani: *Nature* **408**, 944 (2000).
69) L.D. Anh, P.N. Hai and M. Tanaka: *Nature Commun.* **7**, 13810 (2016).
70) H. Ohno, H. Munekata, T. Penney, S. von Molnar and L.L. Chang: *Phys. Rev. Lett.* **68**, 2664 (1992).
71) S. Datta and B. Das: *Appl. Phys. Lett.* **56**, 665 (1990).
72) S. Sugahara and M. Tanaka: *Appl. Phys. Lett.* **84**, 2307 (2004).
73) H. Dery, P. Dalal, L. Cywinski and L.J. Sham: *Nature* **447**, 573 (2007).
74) I. Appelbaum, B. Haung and D.J. Monsma: *Nature* **447** ,295 (2007).
75) B. Huang, H-J. Jang and I. Appelbaum: *Appl. Phys. Lett.* **93**, 162508 (2008).
76) Y. Lu and I. Appelbaum: *Appl. Phys. Lett.* **97**, 162501 (2010).
77) B. Huang, D.J. Monsma and I. Appelbaum: *Phys. Rev. Lett.* **99**, 177209 (2007).
78) T. Sasaki, T. Oikawa, T. Suzuki, M. Shiraishi, Y. Suzuki and K. Tagami: *Appl. Phys. Express* **2**, 053003 (2009).
79) T. Suzuki, T. Sasaki, T. Oikawa, M. Shiraishi, Y. Suzuki and K. Noguchi: *Appl. Phys. Express* **4**, 023003 (2011).
80) T. Sasaki, Y. Ando, M. Kameno, T. Tahara, H. Koike, T. Oikawa, T. Suzuki and M. Shiraishi: *Phys. Rev. Applied* **2**, 034005 (2014).
81) T. Tahara, H. Koike, M. Kameno, T. Sasaki, Y. Ando, K. Tanaka, S. Miwa, Y. Suzuki and M. Shiraishi: *Appl. Phys. Express* **8**, 113004 (2015).
82) M. Kameno et al.: *Appl. Phys. Lett.* **101**, 122413 (2012).
83) M. Kameno et al.: *Appl. Phys. Lett.* **104**, 092409 (2014).
84) M. Shiraishi, Y. Honda, E. Shikoh, Y. Suzuki, T. Shinjo, T. Sasaki, T. Oikawa, K Noguchi and T. Suzuki: *Phys. Rev. B***83**, 241204(R) (2011).
85) Y. Aoki, M. Kameno, Y. Ando, E. Shikoh, Y. Suzuki, T. Shinjo, M. Shiraishi, T. Sasaki, T. Oikawa and T. Suzuki: *Phys. Rev. B***86**, 081201(R) (2012).
86) T. Sasaki, T. Suzuki, Y. Ando, H. Koike, T. Oikawa, Y. Suzuki and M. Shiraishi: *Appl. Phys. Lett.* **104**, 052404 (2014).
87) T. Tahara, Y. Ando, M. Kameno, H. Koike, K. Tanaka, S. Miwa, Y. Suzuki, T. Sasaki, T. Oikawa and M. Shiraishi: *Phys. Rev. B***93**, 214406 (2016).
88) S. Lee, F. Rortais, R. Ohshima. Y. Ando, S. Miwa, Y. Suzuki, H. Koike and M. Shiraishi: *Phys. Rev. B***99**, 064408 (2019).
89) N. Yamashita, Y. Ando, H. Koike, S. Miwa, Y. Suzuki and M. Shiraishi: Phys. Rev. Applied **9**, 054002 (2018).
90) S. Lee, F. Rortais, R. Ohshima. Y. Ando, M. Goto, S. Miwa, Y. Suzuki, H. Koike and M. Shiraishi: *Appl. Phys. Lett.* **116**, 022403 (2020).
91) N. Yamashita, S. Lee, R. Ohshima, E. Shigematsu, H. Koike, Y. Suzuki, S. Miwa, M. Goto, Y. Ando and M. Shiraishi: *AIP Adv.* **10**, 095021 (2020).
92) N. Yamashita, S. Lee, R. Ohshima, E. Shigematsu, H. Koike, Y. Suzuki, S. Miwa, M. Goto, Y. Ando and M. Shiraishi: *Sci. Reports* **11**, 10583 (2021).
93) H. Koike, S. Lee, R. Ohshima, E. Shigematsu, M. Goto, S. Miwa, Y. Suzuki, T. Sasaki, Y. Ando and M. Shiraishi: *Appl. Phys. Express* **13**, 083002 (2020).
94) R. Ishihara, Y. Ando, S. Lee, R. Ohshima, M. Goto, S. Miwa, Y. Suzuki, H. Koike and M. Shiraishi: *Phys. Rev. Applied* **13**, 044010 (2020).
95) E. Shikoh, K. Ando, K. Kubo, E. Saitoh, T. Shinjo and M. Shiraishi: *Phys. Rev. Lett.* **110**, 127201 (2013).
96) S. Lee, H. Koike, M. Goto, S. Miwa, Y. Suzuki, N. Yamashita, R. Ohshima, E. Shigematsu, Y. Ando and M. Shiraishi: *Nature Mater.* **20**, 1228 (2021).
97) S. Dushenko, M. Hokazono, K. Nakamura, Y. Ando, T. Shinjo and M. Shiraishi: *Nature Commun.* **9**, 3118 (2018).
98) S. Yoshitake, R. Ohshima, T. Shinjo, Y. Ando and M. Shiraishi: *Appl. Phys. Lett.* **117**, 092406 (2020).
99) R. Ohshima, Y. Kohsaka, Y. Ando, T. Shinjo and M. Shiraishi: *Sci. Reports* **11**, 21799 (2021).
100) S. Dushenko, M. Koike, Y. Ando, T. Shinjo, M. Myronov and M. Shiraishi: *Phys. Rev. Lett.* **114**, 196602 (2015).
101) A. Yamada, M. Yamada, M. Honda, S. Yamada, K. Sawano and K. Hamaya: *Appl. Phys. Lett.* **119**, 192404 (2021).
102) M. Yamada, F. Kuroda, M. Tsukahara, S. Yamada,

T. Fukushima, K. Sawano, T. Oguchi and K. Hamaya: *NPG Asia Mater.* **12**, 47 (2020).

Received Nov. 17, 2022; Accepted Dec. 14, 2022.

J. Magn. Soc. Jpn., **47**, 38-41 (2023) <Leter>

Improvement of GHz Range Electromagnetic Properties of Ferrite Thin Film Magnetic Core Integrated RF Inductor

T. Nakano*, S. Miyazaki*, Y. Ozaki*, K. Koike*, D. Inokuchi**
* Materials Research Center, TDK Corporation, Narita, Chiba, 286-8588, Japan
** Evaluation & Analysis Center, TDK Corporation, Ichikawa, Chiba, 272-8588, Japan

Ferrite thin film magnetic core integrated radio frequency inductors (RFIs) were investigated in order to realize RFIs with a smaller size, higher driving frequency, and higher quality factor (Q). The ferrite thin films were fabricated by low-temperature spin-spray deposition assuming adaptation to the photolithography process for inductor fabrication with two different compositions: $Ni_{0.16}Zn_{0.20}Fe_{2.64}O_{4+\delta}$ (NZFO) and $Co_{0.11}Fe_{2.89}O_{4+\delta}$ (CFO). The RFI with CFO had a 34% higher inductance and 43% Q improvement compared with the air core RFI at a frequency of 1 GHz. It was confirmed that the complex permeability of the films was correlated with the frequency characteristics of the RFIs with the ferrite thin films. The results suggest that integrating ferrite thin film in RFIs is effective for future mobile device applications.

Key words: Ferrite thin film, Radio frequency inductor, Spin-spray method, Complex permeability, Photolithography

1. Introduction

In recent years, the fifth-generation wireless communication technology (5G) has been used. The electric components used in radio frequency (RF) front-end circuits such as antennas, amplifiers, filters, and inductors must be miniaturized and the driving frequency and quality factor (Q) increased. The air core (non-magnetic material) type of structure is selected for mass-produced RF inductors (RFIs) to satisfy the requirements of cost, inductance tolerance, and high Q. However, to satisfy 5G demands, further improvements to the structure and process of RFIs are required. Therefore, photolithography and Cu plating have been examined for fabricating future RFIs to improve the wire resistance and shape, which can increase Q.

Inserting a magnetic core can solve the above problems and has been studied with various magnetic materials [1)-5)]. The magnetic core must have a high natural resonance frequency (f_r) and electric resistance in order to maintain constant permeability while preventing increasing core loss until the driving frequency of RFIs (ex. 0.45 to 6 GHz for 5G sub-6 bands). Ferrite film is a possible candidate for the magnetic core as it has both shape magnetic anisotropy and a higher electric resistance. Low temperature processes (<100 °C) are also desirable for fabricating the magnetic core assuming adaptation to the photolithography process. Spin-spray deposition, which was proposed by M. Abe et al [6)-8)], is a ferrite thin-film fabrication process that uses a low temperature, requires no vacuum, and has a high deposition rate for various substrates such as glass, silicon, and organic material. However, there have been few reports on ferrite thin film integrated RFIs that compare both RFI and film properties in the GHz bands [3)-5), 8), 9)].

In this work, $Ni_{0.16}Zn_{0.20}Fe_{2.64}O_{4+\delta}$ (NZFO) and $Co_{0.11}Fe_{2.89}O_{4+\delta}$ (CFO) ferrite thin films are fabricated by spin-spray deposition and ferrite thin films integrated RFIs are fabricated, and the electromagnetic properties of both the films and the RFIs are examined.

2. Experimental

2.1 Ferrite thin film deposition

Ferrite thin films with compositions of NZFO and CFO were fabricated by spin-spray deposition as shown in Fig. 1. A reaction solution and oxidizing solution were sprayed simultaneously on rotating substrates heated at selected temperatures between 70 °C and 90 °C. The substrate was selected from a quartz or photoresist coated Si wafer, which is described later. For the

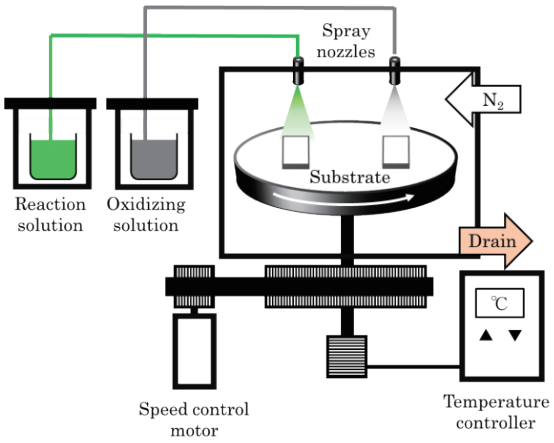

Fig. 1 Schematic images of spin spray deposition.

Corresponding author: T. Nakano (e-mail: Takuma.Nakano@tdk.com).

deposition of NZFO, the reaction solution contained 20 mM $FeCl_2 \cdot 4H_2O$, 5 mM $NiCl_2 \cdot 6H_2O$, and 0.1 mM $ZnCl_2$ in deionized water, and the oxidizing solution contained 5 mM KNO_2 and 65 mM CH_2COONH_4 in deionized water. For the deposition of CFO, the reaction solution contained 20 mM $FeCl_2 \cdot 4H_2O$ and 1 mM $CoCl_2 \cdot 6H_2O$ in deionized water, and the oxidizing solution contained 5-mM KNO_2 and 65 mM $CH_2COONa \cdot 3H_2O$ in deionized water. All reagents were purchased from Wako Pure Chemical Industries.

2.2 Measurement

The film structure and composition were examined by X-ray diffraction (XRD) with Cu Kα and a scanning electron microscope (SEM) after an ion milling polish and inductively coupled plasma mass spectrometry. Magnetization curves were taken on 5 mm × 5 mm samples using a vibrating sample magnetometer (VSM). Complex permeability and f_r were measured using a short-circuited microstrip line (KEYCOM, PER01) [10] with which accuracy of the complex permeability is within 5%, and a flexible microstrip line-type probe [11].

2.3 Inductor fabrication

Solenoid RFIs were fabricated on a Si wafer using a photolithography process and consisted of four parts of Cu components, which were lower wiring, connection via, upper wiring, and upper electrode, as shown in Fig. 2. A 2μm thick ferrite thin film was inserted between the lower and upper wiring for the magnetic core integrated inductors. Each Cu component was fabricated as follows: sputtered Cu seed layer deposition, lapping and patterning of the negative dry film resist (RY-5115 from Showa Denko Materials), Cu electroplating, seed layer and dry film resist removal, and filling of gaps with a permanent photoresist (SU-8 3005 of Nippon Kayaku). The ferrite thin films were patterned into a 400 μm wide × 1000 μm long rectangular bar using photolithography and etched in a 36 wt% HCl solution.

3. Result and discussion

3.1 Film properties

Figure 3 shows cross-sectional SEM images of the ferrite thin films. Dense and >2 μm thick films were achieved. Figure 4 shows out-of-plane XRD spectra. All diffraction peaks corresponded to a spinel structure, and thus, the films were crystalized with low-temperature spin-spray deposition. A structure perpendicular to the substrate surface was confirmed in SEM images, and a crystalline orientation to the (111) plane was also confirmed, which have been reported for other ferrite films fabricated by spin-spray deposition [6].

The values of the saturation magnetization (M_S) and coercivity examined by VSM were 415 emu/cc and 27 Oe for NZFO and 403 emu/cc and 107 Oe for CFO as shown in Fig. 5. It is reported that ferrite thin films fabricated by spin-spray deposition have a higher M_S compared with general bulk ferrites (ex. 300~350 emu/cc for $Ni_{0.5}Zn_{0.5}Fe_2O_4$ [9, 12]) as they contain a large amount of Fe^{2+} [6]. Figure 6 shows the frequency dependences of the complex permeability measured by a short-circuited microstrip line. The values of the real part of complex permeability (μ_r') for the NZFO and CFO were 30 up to 0.5 GHz and 8 up to 2 GHz, respectively, and then both decreased as the frequency increased. The imaginary part of complex permeability (μ_r") for NZFO indicated a broad peak over the entire range of the frequency and

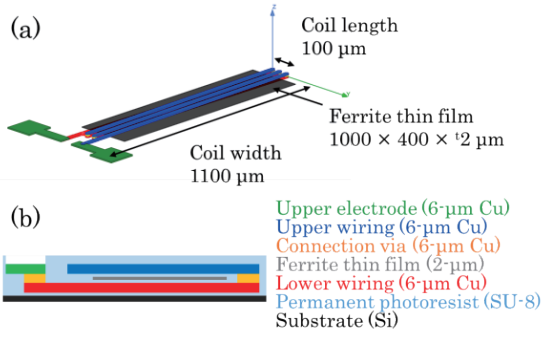

Fig. 2 Schematic images of ferrite thin film integrated RFI with (a) perspective and (b) cross-sectional view.

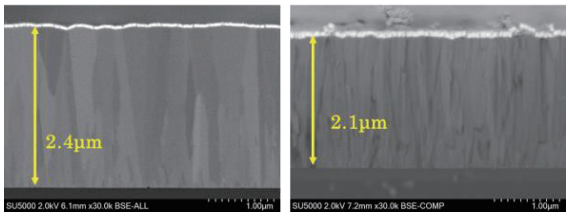

Fig.3 Cross-sectional SEM images of (a) NZFO and (b) CFO.

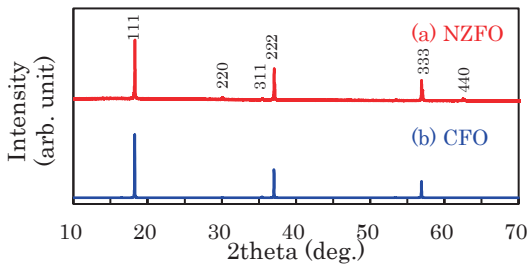

Fig. 4 Out of plane XRD spectra of (a) NZFO and (b) CFO.

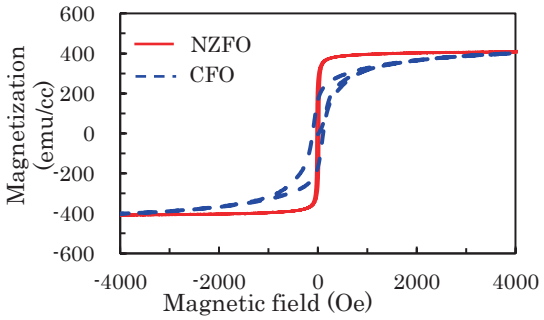

Fig. 5 In plane *M-H* curves of NZFO (red solid line) and CFO (blue dashed line).

contained two peaks, which may suggest the presence of at least two magnetic anisotropy fields and/or domain wall resonance [8), 13)]. The peak of μ_r" for CFO was also broad and observed at around 2 GHz. It is reported that ferrites containing cobalt have a large damping constant (α >0.1) due to a large magnetic anisotropy disarmament magnetoelastic effect [14), 15)]. Low signal to noise ratio around lower frequency (< 0.5 GHz) was caused by sensitivity of vector network analyzer. Peaks of μ_r' and μ_r" around 10 GHz arose from measurement equipment.

Figure 7 shows the relationship between the f_r and static μ_r' of the bulk and film ferrites. The values for the bulk ferrites were evaluated by complex permeability measurement of sintered toroidal cores fabricated by using a conventional solid phase method [16)] with various ferrite compositions. The static μ_r' of the film ferrites are excerpted from μ_r' at 100 MHz in Fig. 6. The values of f_r for the film ferrites were estimated using the following equation based on FMR measurement with various in-plane external magnetic fields using a flexible microstrip line-type probe [17), 18)].

$$f_{\mathrm{FMR}} = \gamma/2\pi\sqrt{(M_s/\mu_0 + H_k + H_{ex})(H_k + H_{ex})}, \quad (1)$$

where f_{FMR} is the ferromagnetic resonance frequency, γ is the gyromagnetic ratio, M_s is the saturation magnetization, μ_0 is the permeability of free space, H_k is the magnetic anisotropy field, and H_{ex} is the external magnetic field. The relationship between the f_r and static μ_r' of the bulk ferrite (solid line in Fig. 7) corresponds to Snoek's limitation rule. The result shows that the relationship of the film ferrite (dotted line) exceeded Snoek's limit for bulk ferrite, with the effect of shape magnetic anisotropy [18)]. This result will need to be further discussed including the modeling of magnetic anisotropy.

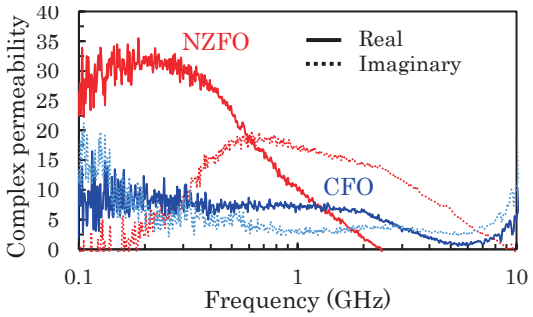

Fig. 6 Frequency dependences of real (solid lines) and imaginary part (dotted lines) of complex permeability of NZFO (red) and CFO (blue).

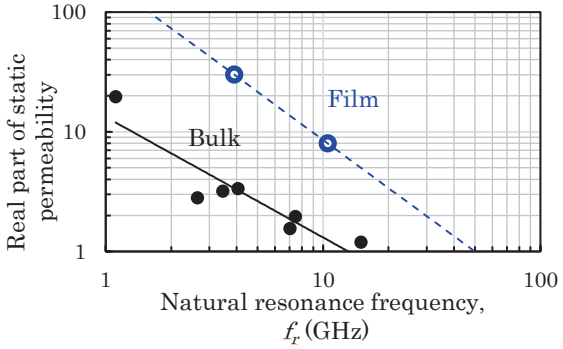

Fig. 7 Relationship between natural resonance frequency and real part of static permeability of bulk (black) and film ferrites (blue).

3.2 Inductor properties

Figure 8 shows top views taken by an optical microscope and cross-sectional views taken by SEM of the air-core and magnetic-core solenoid RFIs. The ferrite thin films were successfully deposited and patterned between the lower and upper wiring with the low temperature process.

The frequency dependence of inductance (L) and Q are shown in Fig. 9. For the air core RFI, the value of L was almost constant up to approximately 3 GHz, and a peak in the self-resonance frequency (SRF) was observed at 10 GHz. By integrating NZFO and CFO, the values of L increased compared with that of the air core RFIs up to 4 and 8 GHz, respectively, and the values of Q increased up to 1 GHz for NZFO and 2 GHz for CFO. Table I summarizes the L and Q values of the fabricated RFIs,

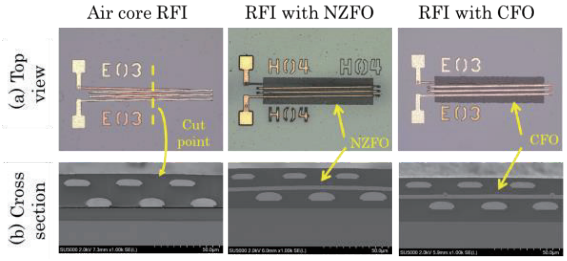

Fig.8 (a) Top and (b) cross-sectional views of air core and magnetic core solenoid RFIs.

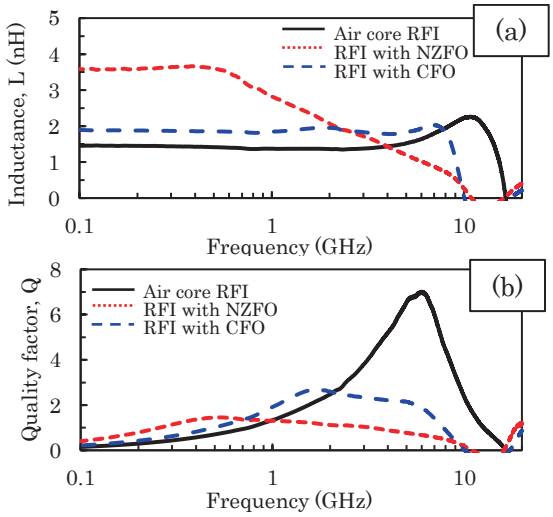

Fig. 9 Frequency dependence of (a) inductance and (b) quality factor of RFIs.

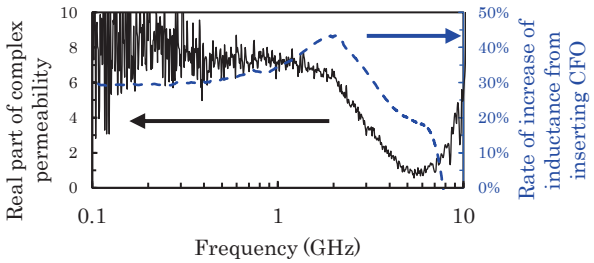

Fig. 10 Comparison of frequency dependence of real part of complex permeability (black, left axis) and rate of increase of inductance from inserting CFO (blue, right axis).

Table I Summary of inductance and quality factor of air core and ferrite thin film integrated RFI.

	Inductance, L (nH)		Quality factor, Q		
	1 GHz	5 GHz	1 GHz	5 GHz	Q_{max}
Air core	1.37	1.52	1.3	6.5	7.0
RFI with CFO	1.84	1.82	1.9	2.1	2.7
ΔV_{CFO}	34%	20%	43%	-67%	-62%
RFI with NZFO	2.82	1.20	1.3	0.8	1.5
ΔV_{NZFO}	106%	-21%	-3%	-88%	-79%

and the rate of increase of L and Q from inserting the ferrite thin films [$\Delta V_{NZFO\ or\ CFO} = (V_{NZFO\ or\ CFO} - V_{air})/V_{air}$, where $V_{NZFO\ or\ CFO}$ is the L or Q of RFI with NZFO or CFO and V_{air} is the L or Q of air core RFI]. The RFI with CFO had a 34% higher inductance and 43% Q improvement compared with the air core RFI at a frequency of 1 GHz. It was confirmed that both GHz-band L and Q are enhanced by integrating ferrite thin films, especially using CFO.

Figure 10 shows a comparison of μ_r' and R_{CFO} of L. The frequency dependences of both decreased as the frequency increased with almost the same slope above 2 GHz. This result indicates that integrating ferrite thin film in RFI is effective for improving RFI properties with GHz bands. In addition, the slope of the dependence of the rate of increase of L was shifted toward higher frequencies compared with the slope of μ_r'. This may be due to the effect of SRF, stress, or deficiencies induced during the RFI process and/or shape difference of CFO samples. The CFO sample for permeability measurement was 5 mm × 5 mm, and that for RFI was 1 mm × 0.4 mm, of which the long side was perpendicular to the solenoid coil length (see Fig. 2). Therefore, there was uniaxial magnetic anisotropy perpendicular to a high frequency magnetic field [1].

4. Conclusion

This paper discussed the electromagnetic properties of ferrite thin film fabricated radio frequency inductors (RFI). Spin-spray deposition and shape patterning of $Ni_{0.16}Zn_{0.20}Fe_{2.63}O_{4+\delta}$ and $Co_{0.11}Fe_{2.89}O_{4+\delta}$ (CFO) were conducted at low temperature (<100°C) assuming adaptation to the photolithography process. The RFI with CFO achieved a 34% higher inductance (L) and 43% quality factor (Q) improvement at a frequency of 1 GHz and superior values for both L and Q up to 2 GHz compared with the air core RFI. Moreover, the frequency dependences of both the real part of complex permeability and L improvement from integrating the ferrite thin film showed a similar trend, which can mean that integrating ferrite thin film is an effective method for future RFI.

Acknowledgements The NZFO film fabrication of this paper was performed by the Matsushita Laboratory at the Tokyo Institute of Technology. The measurement of the high-frequency magnetic properties was performed by Tohoku-TMIT. The authors would like to thank Prof. M. Matsushita of the Tokyo Institute of Technology and Prof. S. Yabukami, Assoc. prof. Y. Endo, and Dr. K. Okita of Tohoku-TMIT for the fruitful discussion.

References

1) A. El-Ghazaly, R. M. White and S. X. Wang: *IEEE Trans. Microw. Theory Tech.*, **65**, 4893 (2017).
2) K. Sato, K. Sugimura, T. Sato, M. Sonehara and H. Takeuchi: *T. Magn. Soc. Jpn. (Special Issues).*, **1**, 44 (2017).
3) N. Sangeneni, N. Bhat, and S. A. Shivashankar: *IEEE 17th Int. Conf. on Nanotech.*, **NANO 2017**, 762 (2017).
4) X. Wang, H. Chen, X. Shi, Y. Gao, H. Lin, J.G. Jones, B.M. Howe, G.J. Brown and N.X. Sun: *AIP Advances*, **7**, 056606 (2017).
5) K. Hagita, Y. Yazaki, Y. Kondo, M. Sonehara, T. Sato, T. Fujii, K. Kobayashi, S. Nakazawa, H. Shimizu, T. Watanabe, Y. Seino, N. Matsushita, Y. Yanagihara, T. Someya, H. Fuketa, M. Takamiya and T. Sakurai: *J. Magn. Soc. Jpn.*, **39**, 71 (2015).
6) N. Matsushita, M. Abe, K. Kondo, S. Yoshida, T. Sato and K. Okada: *J. Surf. Finish. Soc. Jpn.*, **6**, 425 (2010).
7) K. Kondo, S. Yoshida, H. Ono and M. Abe: *J. Magn. Soc. Jpn.*, **101**, 4 (2007).
8) N. Matsushita, T. Nakamura and M. Abe: *IEEE Trans. Magn.*, **38**, 3111 (2002).
9) D. Guo, Z. Zhang, M. Lin, X. Fan, G. Chai, Y. Xu and D. Xue: *J. Phys. D*, **42**, 12 (2009).
10) S. Takeda, T. Hotchi, S. Motomura and H. Suzuki: *J. Magn. Soc. Jpn.*, **39**, 227 (2015).
11) S. Yabukami, K. Nozawa, L. Tonthat, K. Okita and R. Sai: *IEEE Trans. Magn.*, **57**, 1 (2021).
12) N. Hiratsuka, M. Shimizu, M. Fujita and M. Sugimoto: *J. Jpn. Soc. Powder Powder Metallurgy*, **39**, 152 (1992).
13) T. Tsutaoka: J. Appl. Phys, **93**, 2789 (2003).
14) B. Kuanr, S. R. Mishra, L. Wang, D. Delconte, D. Neupane, V. Veerakumar and Z. Celinski: *Mater. Res. Bull*, **76**, 22 (2016).
15) E. L. Verde, G. T. Landi, M. S. Carrião, A. L. Drummond, J. A. Gomes, E. D. Vieira, M. H. Sousa and A. F. Bakuzis: *AIP Advances*, **2**, 032120 (2012).
16) T. Yamaguchi: *J. Jpn. Soc. Powder Powder Metallurgy*, **12**, 62 (1965).
17) C. Kittel: *Phys. Rev.*, **73**, 155 (1948).
18) K. Oota, Jikikougaku no kiso II, Kyoritsu shuppan, Tokyo (1973) (in Japanese).

Received Sep. 15, 2022; Accepted Dec. 13, 2022

J. Magn. Soc. Jpn., **47**, 42-51 (2023) <Paper>

Reluctance Network Model of IPM Motor Representing Dynamic Hysteresis Characteristics for High-Accuracy Iron Loss Calculation Considering Carrier Harmonics

Y. Hane and K. Nakamura
Graduate School of Engineering, Tohoku Univ., *6-6-11 Aoba Aramaki, Aoba-ku, Sendai 980-8579, Japan*

It is essential to establish a simple and practical method for quantitatively estimating the iron loss considering the dynamic hysteresis behavior to further improve the efficiency of electric machines. In a previous study, a novel simple magnetic circuit model representing the dynamic hysteresis characteristics was presented by incorporating a play model, one of the phenomenological dc hysteresis models, and a Cauer circuit, which can consider the skin effect. It was demonstrated that this magnetic circuit model could accurately calculate the hysteresis loops and iron loss even under PMW excitation for magnetic reactors made of several types of core materials in a short time. However, this method can only be used for an object with a simple shape, such as a ring core. Hence, this paper describes that the previously proposed magnetic circuit model is extended to a reluctance network analysis (RNA) to expand the application range. Furthermore, the proposed method was experimentally validated using an interior permanent magnet (IPM) synchronous motor driven by a PWM converter as the examination target.

Key words: interior permanent magnet (IPM) motor, reluctance network analysis (RNA), play model, Cauer circuit, dynamic hysteresis characteristics

1. Introduction

In recent years, the efficiency improvement of electric machines, especially an electric motor, has been strongly desired from the viewpoint of global environmental protection and energy conservation. Among a variety of electric motors, utilization of an interior permanent magnet (IPM) synchronous motor has been dramatically increasing because of its high torque density and efficiency characteristics. To further enhance the performance of an IPM motor, it is necessary to optimally design not only a motor structure but also a whole motor drive system. However, in many cases of machine design using a finite element method (FEM), it takes a lot of calculation time and computer memory so that the coupled analysis with an external driving circuit and a motion equation is not necessarily easy.

To overcome this issue, a reluctance network analysis (RNA) has been proposed so far [1], simulating flux distribution inside an analytical object by expressing it as one reluctance network. In the RNA, all the reluctances are determined by the magnetic properties of materials and dimensions of divided elements. The RNA can be one of the practical solutions because of several advantages, such as a straightforward analytical model, short calculation time, relatively high calculation accuracy, and easy coupling with an external driving circuit and a motion equation. In previous studies, the RNA has been utilized for characteristic calculations of various electric machines, including an SPM motor [2)-4)]. Moreover, although there are very few studies on the derivation of the RNA model for an IPM motor [5)] because of its complicated flux distribution, Ref. 6) indicated the modeling technique of the RNA model for an IPM motor with a relatively small number of divided elements. However, Ref. 6) indicated that the conventional RNA model cannot calculate the iron loss with sufficiently high accuracy because carrier harmonics generated by PWM voltage excitation cannot be considered. Since an IPM motor is generally driven by a PWM converter, it is essential to accurately calculate the iron loss even under a complicated exciting waveform.

In previous studies, a novel RNA model incorporating a play model [7)], which is one of the phenomenological dc hysteresis models, was presented [8)–10)]. The play model can express an arbitrary hysteresis loop with not only high accuracy but also high speed. Although the play model generally requires a lot of measured dc hysteresis loops with various flux density amplitudes, the dc hysteresis loops calculated by a simplified Landau-Lifshitz-Gilbert (LLG) equation [11)], which is one of the physical hysteresis models, can be substituted for the measured ones [12)]. The calculation accuracy of the previously proposed RNA model has been experimentally proved by analyzing various devices, including an SPM motor [8)-10)]. However, all the above studies are limited to characteristic calculations under simple excitation conditions such as sinusoidal and square waveforms. In this model, the calculation accuracy of iron loss is insufficient under PWM excitation because the influence of the skin effect caused by carrier harmonics is neglected.

One of the most attractive eddy current loss models in recent years is a Cauer circuit [13), 14)], which expresses the frequency characteristic of complex permeability by

Corresponding author: Y. Hane (e-mail: yoshiki.hane.e2@tohoku.ac.jp).

a ladder-type electric equivalent circuit composed of multiple resistance and inductance elements. Using the Cauer circuit, the one-dimensional electromagnetic field analysis can be performed with minimal calculation time and cost. Moreover, Ref. 15) indicated that the play model can be combined with the Cauer circuit by excluding the first inductance element. Furthermore, in Ref. 16), a novel simple magnetic circuit model representing the dynamic hysteresis characteristics was presented, incorporating the play model and the Cauer circuit (converted to a magnetic circuit). Using the previously proposed magnetic circuit model, it is possible to accurately calculate hysteresis loops and iron loss even under PWM excitation for ring cores made of several core materials in a short calculation time [16]. However, it is difficult to apply this model to analyze a device with a complicated flux distribution, including an IPM motor.

Therefore, this paper describes that the simple magnetic circuit model proposed in Ref. 16) is extended to the RNA model. The proposed RNA model is experimentally validated by using an IPM motor driven by a PWM converter as the examination target. It was proven that the iron loss could be accurately estimated by taking carrier harmonics under PWM excitation into account with a reasonable calculation time.

2. Previously Proposed Simple Magnetic Circuit Model Representing Dynamic Hysteresis Characteristics

This chapter describes a principle of the previously proposed simple magnetic circuit model representing the dynamic hysteresis characteristics [16], as shown in Fig. 1, which is the basis of the proposed RNA model described later. In the following, it is explained how to represent each component in this model.

Firstly, the dc hysteresis characteristics are expressed by the play model [7], which can represent an arbitrarily shaped hysteresis loop by combining the multiple play hysterons with different widths and the shape function. Here, the magnetic flux density B is the input and the dc hysteresis component of magnetic field H_{dc} is the output, respectively. The behavior of the play model can be described by the following equations:

$$p_j(B,\varsigma_j) = \max\left(\min\left(p_{j0}(B,\varsigma_j), B+\varsigma_j\right), B-\varsigma_j\right) \tag{1}$$

$$H_{dc} = \sum_{j=1}^{N} f_j\left(p_j(B)\right) \tag{2}$$

where an integer from 1 to N is j, the play hysterons at current time step and 1 time step ago are p_j and p_{j0}, a width of the play hysteron is ζ_j, the shape function is f_j, respectively. The values of play hysterons are overwritten at each time step. Although the derivation of the shape function generally requires many measured dc hysteresis loops with various flux density amplitudes, they can be substituted by the calculated ones acquired from the simplified LLG equation [11] so that only a few dc hysteresis loops have to be measured [12]. Fig. 2 shows the comparison of the measured dc hysteresis loops and calculated ones obtained from the simplified LLG equation of non-oriented electrical steel (NOES), whose thickness is 0.35 mm. In the experiment, ac hysteresis loops at a very low frequency of f = 5 Hz were regarded as dc ones. As shown in Fig. 2, the measured and calculated values agree with each flux density amplitude. In addition, as shown in Fig. 3, many dc hysteresis loops used for deriving the play model can be acquired by using the simplified LLG equation without experiment.

Secondly, the classical eddy current loss is represented by a ladder-shaped part composed of repeatedly connected magnetic circuit elements, which is equivalent to the part of the first resistance element and after in the original Cauer circuit [13), 14)], as shown in Fig. 4. This part represents the frequency characteristic of complex permeability due to the skin effect in the physical meaning. The parameters R_m and L_m are defined as follows:

$$R_m = \frac{1}{L}\cdot\frac{l}{S} = \frac{1}{\mu}\cdot\frac{l}{S} \tag{3}$$

$$L_m = R\cdot\frac{l}{S} = \frac{\sigma d^2}{4}\cdot\frac{l}{S} \tag{4}$$

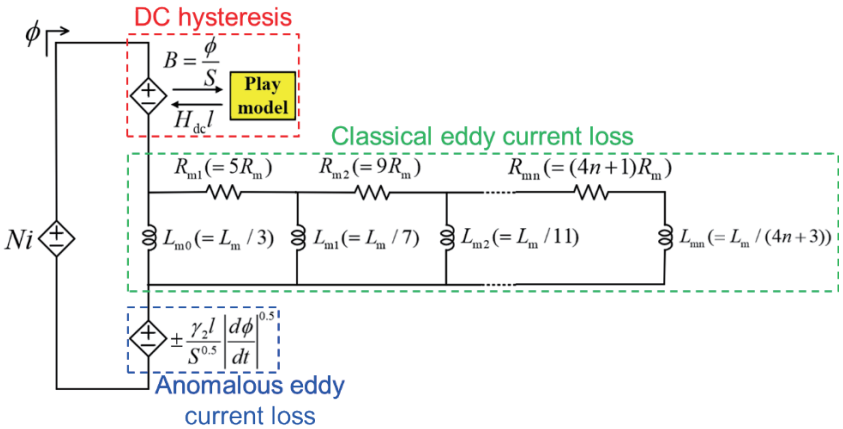

Fig. 1 Previously proposed simple magnetic circuit model representing the dynamic hysteresis characteristics.

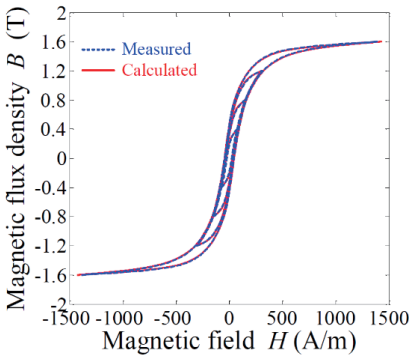

Fig. 2 Comparison of the measured and calculated dc hysteresis loops of NOES.

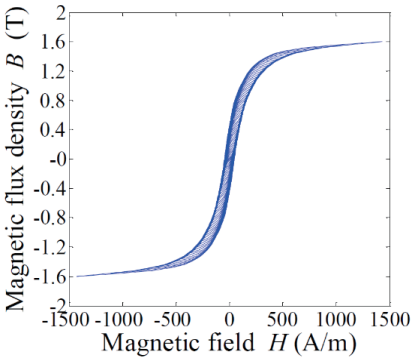

Fig. 3 Calculated dc hysteresis loops of NOES with flux density amplitudes from B_m = 0.04 T to 1.6 T at intervals of 0.04 T.

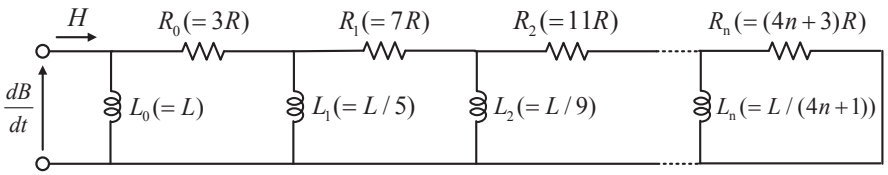

Fig. 4 Original Cauer circuit.

where the coefficients of the original Cauer circuit are L and R, the magnetic path length is l, the average cross-sectional area is S, the permeability is μ, the conductivity is σ, and the thickness of a steel sheet is d, respectively.

Thirdly, the anomalous eddy current loss is represented by a dependent-source element, which outputs the magnetomotive force (MMF) proportional to the input $|d\phi/dt|^{0.5}$. Its coefficient γ_2 can be determined by approximating the measured core loss curves of the material by the least squares method, as shown in Fig. 5, using the following equation [17]:

$$\frac{W_i}{f} = const. + \frac{\pi^2 \sigma d^2 B_m^2}{6 q_i} f + 8.763 \frac{\gamma_2 B_m^{1.5}}{q_i} f^{0.5} \qquad (5)$$

where the iron loss is W_i, the frequency is f, the maximum flux density is B_m, and the mass density of core material is q_i, respectively.

3. Conventional and Proposed RNA Models of IPM Motor Representing Dynamic Hysteresis Characteristics

Fig. 6(a) and (b) show specifications and a rotor structure of an IPM motor with polar anisotropic bonded

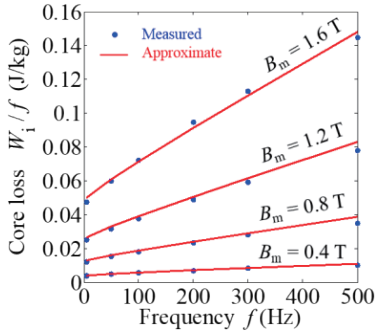

Fig. 5 Measured core loss curves and their approximate curves of NOES.

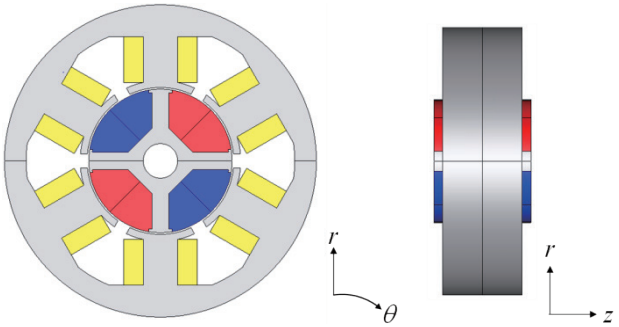

(a) external view

(b) specifications

Diameter	54 mm
Stack length of stator	16 mm
Stack length of rotor	19.5 mm
Gap length	0.3 mm
Number of turns/pole	24 turns/pole
Winding diameter	1.2 mm
Magnet pole pairs	2
Material of magnet	Bonded Nd-Fe-B
Material of iron core	35A300

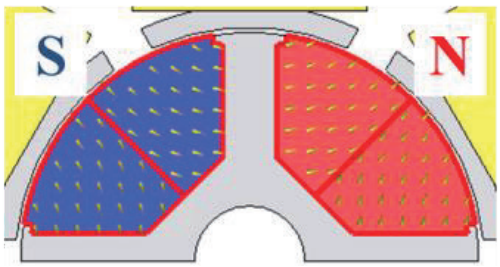

(c) rotor structure

Fig. 6 IPM motor used in the consideration.

Nd-Fe-B magnets used in the consideration. The relative recoil permeability and coercive force of magnets are 1.275 and 461 kA/m, respectively. Also, as shown in Fig. 6(b), rotor magnets are magnetized in not the general radial or parallel directions but the arcuate one.

In the following, it is described how to construct the conventional and proposed RNA models. Firstly, an analytical object is divided into a multiple number of elements. Then, each divided element is replaced with a unit magnetic circuit composed of three or four reluctances, as shown in Fig. 7. The stator core is divided into six regions in the circumferential direction (excluding stator pole tips), which is the same number as slots. On the contrary, stator pole tips, air gaps, and a rotor are divided into 360 elements in increments of 1 degree in the circumferential direction since their flux distribution is more complicated than that of stator poles and yoke. Here, the analytical model is halved in the *r*- and *z*-axis directions, respectively, considering flux distribution symmetry.

Figs. 8 and 9 show the conventional and proposed RNA models of one stator pole of an IPM motor (simplified schematic). The difference between these two models is the method for giving the reluctances in a stator core. In the conventional RNA model, each reluctance in a stator core is determined by approximating the initial magnetization curve of the core material as shown in Fig. 10, using the following equations [6]:

$$H = \alpha_1 B + \alpha_m B^m \tag{6}$$

$$f_m = \left(\frac{\alpha_1 l}{S} + \frac{\alpha_m l}{S^m} \phi^{m-1} \right) \phi \tag{7}$$

$$R_{mc} = \frac{\alpha_1 l}{S} + \frac{\alpha_m l}{S^m} \phi^{m-1} \tag{8}$$

where the coefficients are α_1 and α_m, the order is m, the MMF is $f_m = Hl$, the magnetic flux is $\phi = BS$, and the nonlinear reluctance is R_{mc}, respectively. In addition, to calculate the iron loss, the magnetic inductance element given by the following equation should be connected in series with each reluctance given by Eq. (9):

$$L_{mc} = \frac{\beta_1 l}{S} \tag{9}$$

where the coefficient is β_1, which can be determined by approximating the following equation using the least

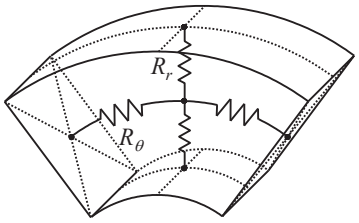

Fig. 7 Unit magnetic circuit.

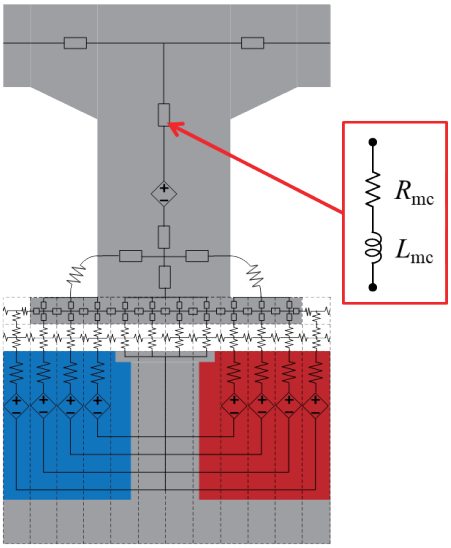

Fig. 8 Simplified schematic diagram of the conventional RNA model of one stator pole of an IPM motor.

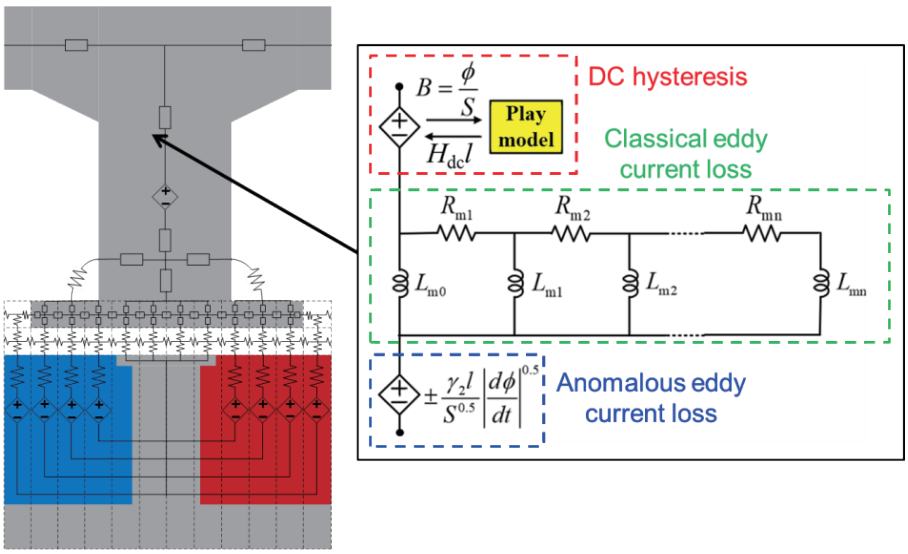

Fig. 9 Simplified schematic diagram of the proposed RNA model of one stator pole of an IPM motor representing the dynamic hysteresis characteristics.

square method:

$$W_i = \frac{2\pi^2 \beta_1}{q_i} f^2 B_m{}^2 \quad (10)$$

In this way, the iron loss can be simply calculated with the accuracy equivalent to the Steinmetz's empirical equation [18] without the post-processing in the RNA [6]. However, its calculation accuracy is not sufficiently high under PWM excitation. On the other hand, in the proposed RNA model, each reluctance denotes the dc hysteresis characteristics by the play model, the classical eddy current loss by a ladder-shaped part composed of inductance and resistance elements, which is equivalent to the Cauer circuit, and the anomalous eddy current loss by a dependent-source, respectively, in each divided element. Here, when a ladder-shaped part is truncated at 1st stage, the proposed method is equivalent to the previous one presented in Refs. 8)–10). Besides, the MMF generated from the armature winding current is concentrated at the center of each stator pole, where the armature winding is applied [6]. In contrast, the reluctances in a rotor core are regarded as zero, that is, these magnetic paths are short-circuit in this model because these reluctances are extremely smaller than those in magnets [6] so that the calculation accuracy of the reluctance torque is not affected in this way.

Next, the reluctances in air gaps and air region surrounding a stator core, where the leakage flux flows from each stator pole, can be expressed by the following equation [6]:

$$R_a = \frac{l}{\mu_0 S} \quad (11)$$

where the vacuum permeability is μ_0.

Moreover, the reluctance R_p and the MMF F_c in a rotor magnet are connected in series in each element of a magnet and given by the following equation [6]:

$$R_p(\theta) = \frac{|l_p(\theta)|}{\mu_0 \mu_r S} \quad (12)$$

$$F_c(\theta) = H_c l_p(\theta) \quad (13)$$

where the relative recoil permeability is μ_r and the coercive force is H_c, respectively. In addition, the effective magnet length in the arc-shaped magnetized direction is $l_p(\theta)$, which changes corresponding to a rotor position angle θ, as shown in Fig. 11(a) and (b). Here, $l_p(\theta)$ can be approximately given by the following Fourier series [6]:

$$l_p(\theta) = \sum_{j=1}^{N} a_j \cos 2(2j-1)\theta \quad (14)$$

where arbitrary coefficients are a_j and N = 15, respectively. In this manner, even the generally complicated flux distribution of an IPM motor can be expressed by a simple model with a minimum number of elements compared with a finely divided FEM model.

Further, when an analytical object has an overhang structure, a 3-D analytical model is generally adopted to simulate the flux distribution strictly. However, here, to avoid an increase in the calculation time as the RNA model scales up, this structure is expressed by connecting each circumferential element in protruding rotor magnets and the lamination plane on stator pole tips facing each other, and the reluctances which leakage flux flows from all the other elements in the circumferential direction, as shown in Fig. 12 [6].

4. Simulation Results by Using Conventional and Proposed RNA Models

In this chapter, the above-derived RNA model is used for the characteristic calculation of an IPM motor to validate the proposed method. The RNA is performed using Ansys Twin Builder 2021 R1, one of the general-purpose circuit simulators. The validity of the calculation results is proved by comparing them with the experimental ones, which are acquired by measuring input current and power under variously loaded conditions (the load torque of from 0 mN·m to 200 mN·m

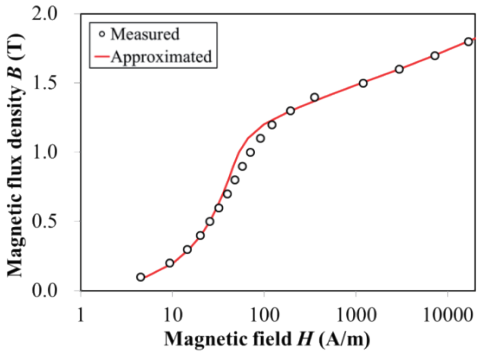

Fig. 10 *B-H* curve of core material and its approximated curve.

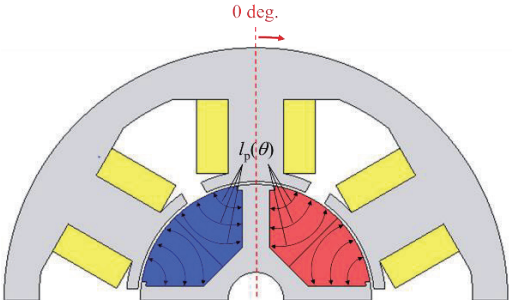

(a) where $l_p(\theta)$ points

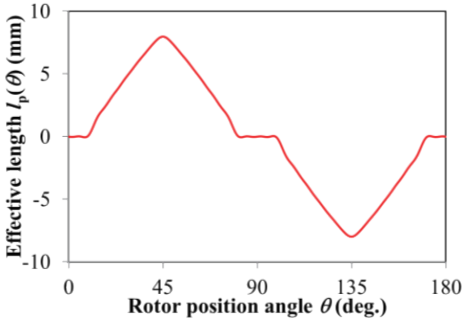

(b) relationship between the rotor position angle θ and the effective length $l_p(\theta)$

Fig. 11 Effective length $l_p(\theta)$ of the permanent magnet corresponding to the rotor position angle θ.

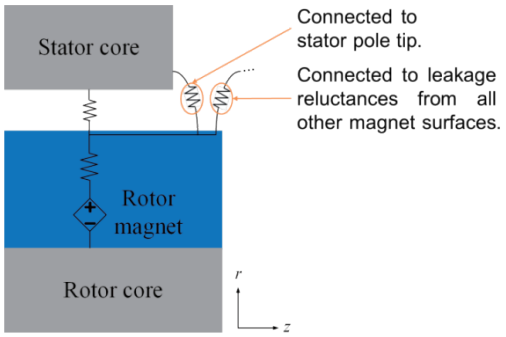

Fig. 12 Magnetic circuit in an overhang part.

at intervals of 20 mN·m) while driven by a PWM converter at the constant rotational speed of 12600 rpm, using the experimental system shown in Fig. 13. In the analysis, the measured exciting current waveforms, whose carrier frequency is 20 kHz and current phase angle is 18 deg., are input. Fig. 14(a) and (b) show examples of the measured exciting current waveforms.

4.1 Simulation results by using conventional RNA model

In this section, the conventional RNA model described in the chapter 3 is analyzed before the proposed one, to point out its challeges. For reference, the RNA model is analyzed is performed by inputting the ideal sinusoidal ones with the rms values of 0 A to 7 A at intervals of 1 A, in addition to the measured ones mentioned above. The parameters of magnetic circuit elements are $\alpha_1 = 51$, $\alpha_m = 2.5$, $m = 15$, and $\beta_1 = 0.0438$, respectively. Moreover, the FEM model of an IPM motor is also analyzed under sinusoidal excitation as well, using JMAG-Designer Ver. 20.0, one of the general-purpose electromagnetic field analysis software.

Fig. 15 shows the comparison of the measured and calculated winding rms current density versus torque characteristics. In the analysis, the torque is calculated by using the following equation, with a very thin torque calculation layer of 10 μm provided on the rotor surface as shown in Fig. 16 [6), 19)]:

$$\tau_m = \frac{2n_\theta}{\pi}\sum_{j=1}^{n_\theta} f_{s\theta j}\phi_{srj} \qquad (15)$$

where the number of divided elements in the circumferential direction is n_θ, the MMF of each element on the rotor surface generated in the circumferential direction is $f_{s\theta j}$, and the flux of each element on the rotor surface flowing in the radial direction is f_{srj}, respectively. In addition, the calculated values are corrected by subtracting the loss torque value due to the measured mechanical loss, which cannot be considered in the analysis. Here, the values of the measured mechanical loss and its loss torque are 5.8 W and 4.4 mN·m, respectively, at 12600 rpm. From the figure, it is clear that the calculated values of the RNA when excited by the measured current waveforms are in good agreement with the measured ones, while the calculated values for the RNA and the FEM under sinusoidal excitation have a little errors with respect to the measured ones due to

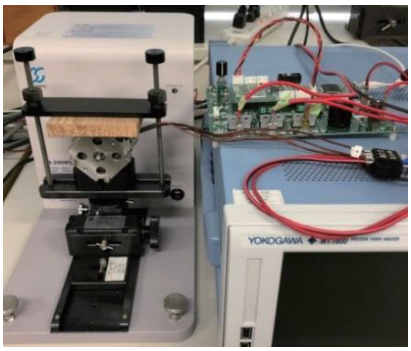

Fig. 13 Experimental setup.

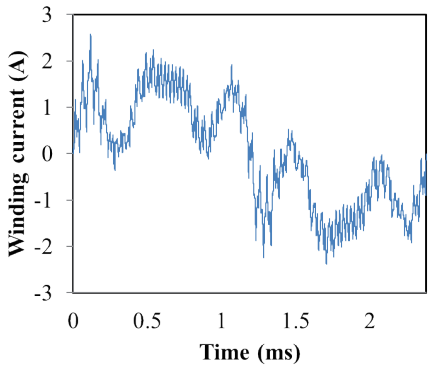

(a) load torque is 20 mN·m

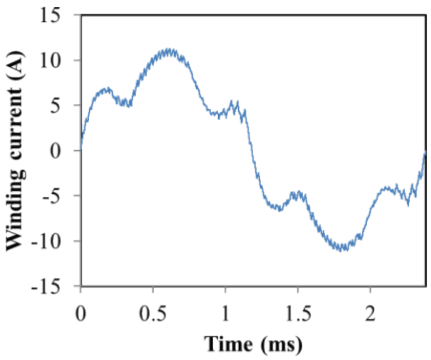

(b) load torque is 200 mN·m

Fig. 14 Measured exciting current waveforms input in the analysis.

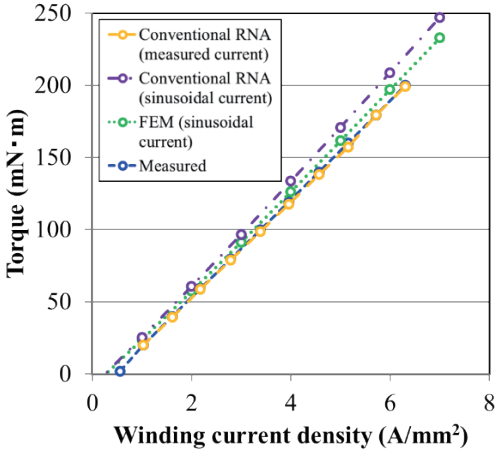

Fig. 15 Comparison of the measured and calculated winding rms current density versus torque characteristics (conventional RNA model).

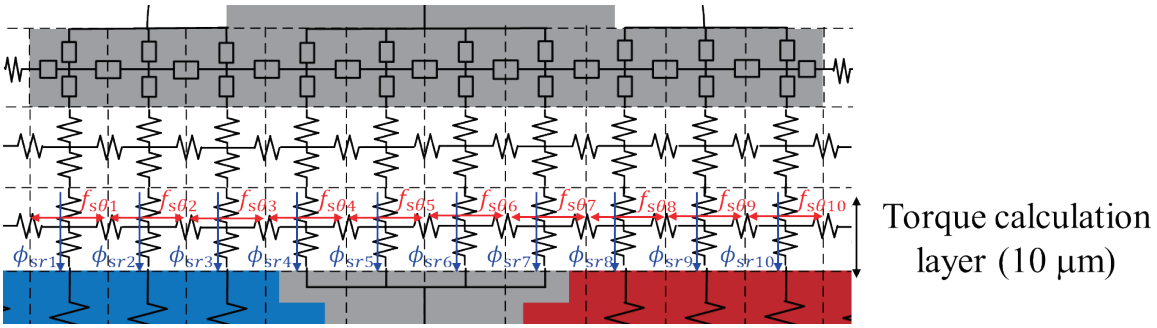

Fig. 16 Enlarged view of the rotor surface of the RNA model.

the low-order harmonic components included in the measured current waveforms as shown in Fig. 14.

Fig. 17 shows the comparison of the measured and calculated iron loss characteristics. In the FEM, the iron loss is obtained using the Steinmetz's empirical equation for post-processing [18]. In the experiment and analysis, the iron loss is acquired by subtracting the machine output, copper loss, and mechanical loss (only for the measurement) from the electrical input. Since almost no eddy current is generated in the bonded magnet, the magnet eddy current loss is regarded as zero. From the figure, it is understood that the calculated values for the RNA and the FEM under sinusoidal excitation are underestimated compared with the measured ones since the carrier harmonics are not taken into consideration. On the contrary, the calculated values of the RNA when excited by the measured current waveforms are overestimated compared with the measured ones since the dependence of the minor loop loss on the dc flux component and the skin effect are not considered.

Fig. 18 shows the comparison of the measured and calculated efficiency characteristics. The calculation values are obtained, including the measured mechanical loss. As shown in the figure, due to the errors in the torque and iron loss characteristics mentioned above, the calculated values for the RNA and the FEM under sinusoidal excitation are a little overrated while the calculated values of the RNA when excited by the measured current waveforms are underrated, compared with the measured ones.

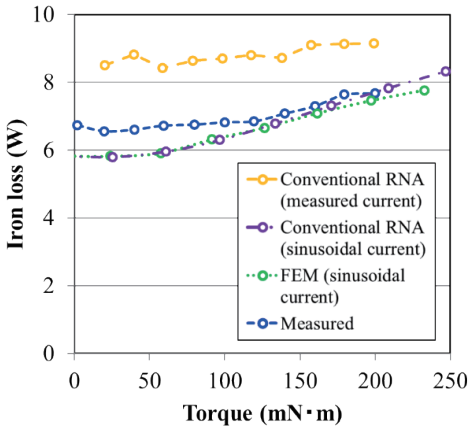

Fig. 17 Comparison of the measured and calculated iron loss characteristics (conventional RNA model).

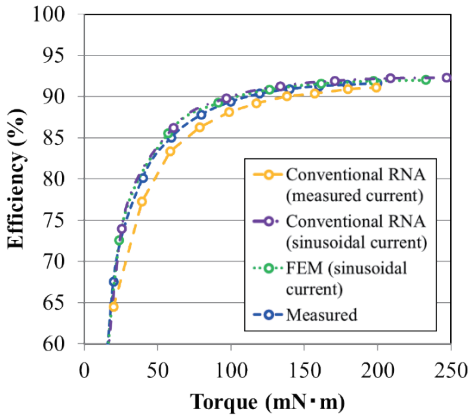

Fig. 18 Comparison of the measured and calculated efficiency characteristics (conventional RNA model).

4.2 Simulation results by using proposed RNA model

In this section, the validity of the proposed RNA model is experimentally verified. The analysis is performed by exciting the measured current waveforms shown in Fig. 14. Moreover, a ladder-shaped part is truncated in the analysis at the first, second, or third stages, that is, L_{m0}, L_{m1}, or L_{m2}, respectively. The parameters of magnetic circuit elements are $\sigma = 2.2\times10^{6}$, $d = 3.5\times10^{-4}$, and $\gamma_2 = 0.467$, respectively. Besides, the parameter μ is approximately given by the instantaneous value of the differential permeability on the centerline of a dc hysteresis loop [16].

Fig. 19(a) – (c) show the comparison of the measured and calculated winding rms current density versus torque characteristics. In the analysis, the torque is calculated by using Eq. (15). From the figures, it is clear that the measured and calculated results are in good agreement regardless of the number of ladder stages.

Fig. 20(a) – (c) show the comparison of the measured and calculated iron loss characteristics. As shown in the figures, the calculated values are closer to the measured ones as the number of ladder stages increases. It is clear that both results are almost in good agreement when a ladder circuit has three stages. However, there is still a possibility that the proposed model will improve the calculation accuracy because slight errors can be seen at low load conditions when carrier harmonics are larger. Possible causes of these errors seem to be methods for giving the parameter μ [16] and expressing the anomalous eddy current loss, and neglect of the rotational magnetic

field [20] and the edge effect [21].

Fig. 21(a) – (c) show the comparison of the measured and calculated efficiency characteristics. These figures reveal that the measured and calculated values are in good agreement when a ladder circuit has 2 stages or more.

Furthermore, Fig. 22 shows an example of the calculated hysteresis loop in a stator core obtained from the proposed RNA model. This figure indicates that the proposed method can draw such a local complicatedly distorted hysteresis loop due to PWM excitation, even though the dynamic hysteresis behavior inside of a core is generally difficult to acquire by the experiment and analysis. Its calculation accuracy should be verified by the experiment (such as the *H*-coil method) in the future.

Finally, Table 1 shows the calculation time of the proposed method per one cycle of electric angle for each case. Here, the PC used for the analysis has a 12-core CPU and 48 GB of memory, respectively, and the analysis is performed non-parallel. From the table, it can be seen that the proposed model can perform the iron loss analysis under PWM excitation considering carrier harmonics in a reasonable time. In addition, in Ref. 6), it is indicated that the FEM takes about 217 times longer calculation time than the RNA when analyzing the same analytical object. Therefore, if this

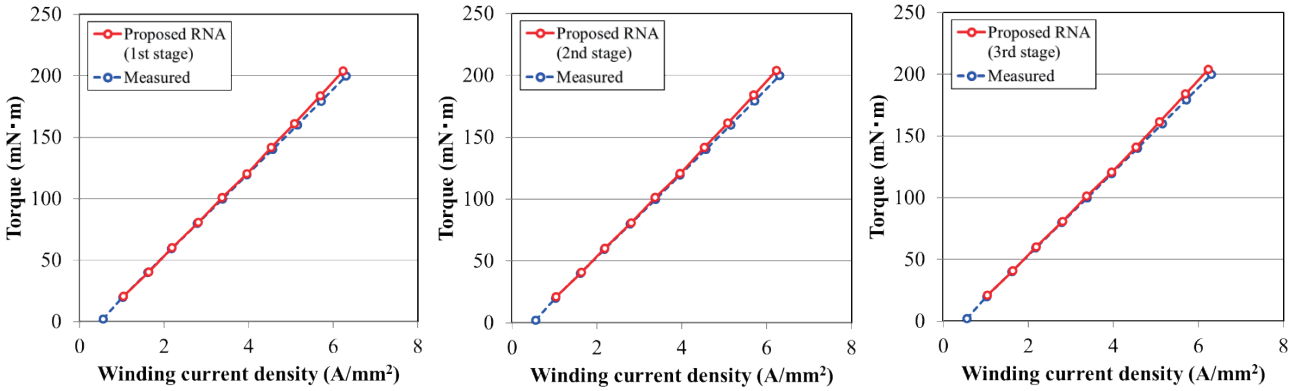

(a) truncated at the 1st stage (b) truncated at the 2nd stage (c) truncated at the 3rd stage

Fig. 19 Comparison of the measured and calculated winding rms current density versus torque characteristics (proposed RNA model).

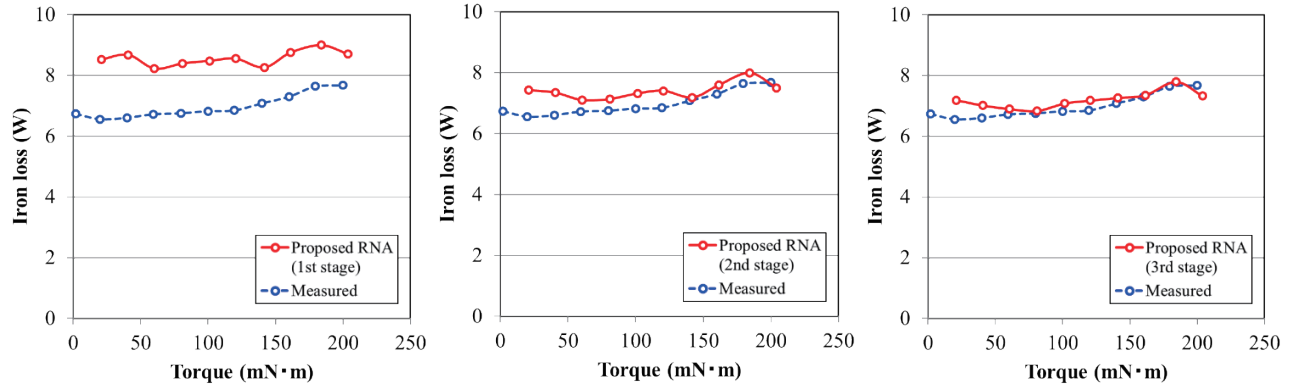

(a) truncated at the 1st stage (b) truncated at the 2nd stage (c) truncated at the 3rd stage

Fig. 20 Comparison of the measured and calculated iron loss characteristics (proposed RNA model).

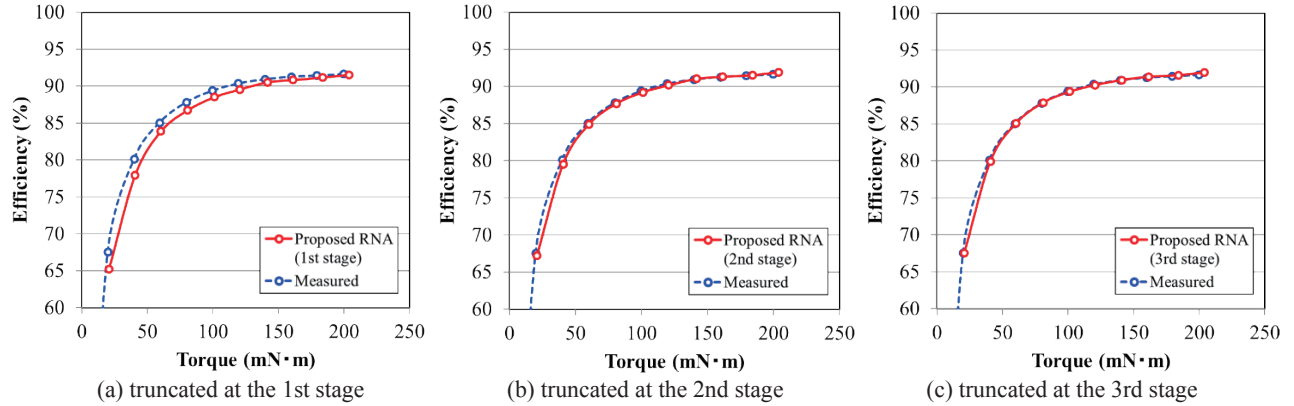

(a) truncated at the 1st stage (b) truncated at the 2nd stage (c) truncated at the 3rd stage

Fig. 21 Comparison of the measured and calculated efficiency characteristics (proposed RNA model).

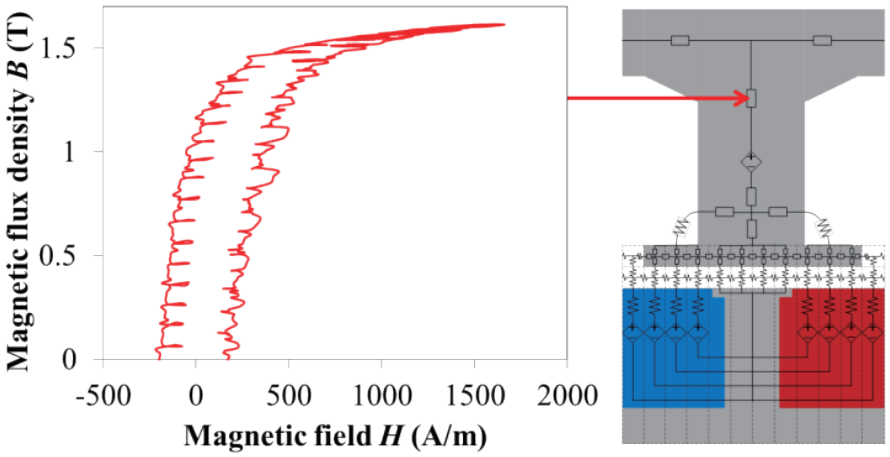

Fig. 22 Calculated hysteresis loop in the element of a stator core of the proposed RNA model.

Table 1 Calcalation time per one cycle of the RNA.

Torque (mN・m)	1st stage (h)	2nd stage (h)	3rd stage (h)
20	4.6	8.1	10.2
40	4.5	8.1	10.0
60	4.9	8.2	10.2
80	4.9	8.2	10.1
100	4.7	8.1	10.1
120	4.8	7.9	9.9
140	4.7	8.0	9.8
160	4.8	7.7	9.6
180	4.6	7.7	9.6
200	4.1	7.8	9.7

motor is analyzed by the FEM in consideration of the dynamic hysteresis characteristics, the estimated calculation time per cycle is 891 hours in the shortest case and 2217 hours in the longest case, which suggests that there is a huge practical problem.

5. Conclusion

This paper described that a novel RNA model is derived by incorporating the play model and Cauer circuit to represent the dynamic hysteresis characteristics. The novelties in this paper are as follows:

(1) Based on the RNA, a device with a complicated flux distribution, such as an IPM motor, can be analyzed by taking the dynamic hysteresis characteristics including the skin effect into consideration, which has not been achieved in Refs. 8)–10) and 16).

(2) The calculation accuracy of the proposed RNA model representing the dynamic hysteresis characteristics is examined by comparing the calculated results with the measured ones when an IPM motor is driven by a PWM converter, which has not been achieved in Ref. 22). As a result of the examination, it became clear that the proposed RNA model can calculate the iron loss characteristic with higher accuracy by considering the influence of carrier harmonics, as the number of ladder stages is larger. Also, the proposed model can accurately calculate the torque and efficiency characteristics regardless of the number of ladder stages.

(3) The proposed RNA model can draw a local complicatedly distorted hysteresis loops inside a core, which is difficult to measure and calculate in general.

(4) The calculation time and cost of the proposed RNA model are practical, which has not been achieved in Ref. 22), while it is estimated that a considerable amount of calculation time is required in the FEM.

In the future, we plan to further increase the calculation accuracy of the current RNA model by identifying the causes of errors at low load conditions and experimentally validate the local hysteresis loops inside of an iron core.

Acknowledgements This work was supported by JSPS KAKENHI Grant number JP22K14232 and research grant from Japan power Academy.

References

1) K. Nakamura and O. Ichinokura: *IEEJ Trans. FM*, **128**, 506 (2008).
2) K. Nakamura, K. Kimura, and O. Ichinokura: *J. Magn. Magn. Mat.*, **290-291**, 1309 (2005).
3) M. Fukuoka, K. Nakamura, and O. Ichinokura: *IEEE Trans. Magn.*, **47**, 2414 (2011).
4) K. Nakamura, K. Honma, T. Ohinata, K. Arimatsu, T. Shirasaki, and O. Ichinokura: *J. Magn. Soc. Jpn.*, **38**, 174 (2014).
5) Y. Kano and N. Matsui: *IEEE Trans. Ind. Appl.*, **44**, 543 (2008).
6) Y. Hane, Y. Uchiyama, and K. Nakamura: *J. Magn. Soc. Jpn.*, **45**, 125 (2021).
7) S. Bobbio, G. Miano, C. Serpico, and C. Visone: *IEEE Trans. Magn.*, **33**, 4417 (1997).
8) Y. Hane and K. Nakamura: *Proc. IEEE Int. Magn. Conf. (INTERMAG 2018)*, 1800038 (2018).
9) Y. Hane, K. Nakamura, T. Ohinata, and K. Arimatsu: *IEEE Trans. Magn.*, **55**, 8401306 (2019).
10) Y. Hane, K. Mitsuya, and K. Nakamura: *Proc. IEEE Int. Magn. Conf. (INTERMAG 2021)*, 2100016 (2021).
11) H. Oshima, Y. Uehara, K. Shimizu, K. Inagaki, A. Furuya, J. Fujisaki, M. Suzuki, K. Kawano, T. Mifune, T. Matsuo, K. Watanabe, and H. Igarashi: *J. Jpn. Soc. Pwdr. Metall.*, **61**, S238 (2014).
12) H. Tanaka, K. Nakamura, and O. Ichinokura: *J.Phys.: Conf. Ser.*, **903**, 012047 (2017).
13) Y. Shindo and O. Noro: *IEEJ Trans. FM*, **134**, 173 (2014).

14) Y. Shindo, A. Kameari, and T. Matsuo: *IEEJ Trans. PE*, **137**, 162 (2017).
15) Y. Shindo, T. Miyazaki, and T. Matsuo: *IEEE Trans. Magn.*, **52**, 6300504 (2016).
16) Y. Hane and K. Nakamura: *IEEE Trans. Magn.*, **58**, 7300412 (2022).
17) G.Bertotti: *IEEE Trans. Magn.*, **24**, 621 (1988).
18) C. P. Steinmetz: *Proc. IEEE*, **72**, 197 (1984).
19) K. Nakamura and O. Ichinokura: *Int. Power Electron. Motion Contr. Conf. (EPE-PEMC 2008)*, 441 (2008).
20) E. Dlala, A. Belahcen, and A. Arkkio: *Physica B*, **403**, 428 (2008).
21) L. Cheng, S. Sudo, Y. Gao, H. Dozono, and K. Muramatsu: *IEEE Trans. Magn.*, **49**, 1969 (2013).
22) O. Messal, F. Dubas, R. Benlamine, A. Kedous-Lebouc, C. Chillet, and C. Espanet: Preprints (2017).

Received Sep. 19, 2022; Revised Nov. 2, 2022; Accepted Nov. 22, 2022

J. Magn. Soc. Jpn., **47**, 52-56 (2023) <Paper>

Magnetic Moment Method with the Idea of Magnetic Surface Charge Method

H. Yano, and K. Sugahara*
ELF Corporation, *3-5-24 Miyahara, Yodogawa, Osaka 532-0003, Japan*
*Faculty of Science and Engineering, Kindai Univ., *3-4-1 Kowakae Higashiosaka 577-8502, Japan*

Magnetic Moment Method (MMM) is well known for its "lightweight" and simplicity of implementation; however, meshing must be carefully treated to obtain accurate results. In this paper, the MMM with the idea of the Magnetic Surface Charge method is proposed that is free from the meshing problem. Accelerator magnets; a C-shaped dipole and a quadrupole magnet, are analyzed, and it is shown that the proposed method outperforms currently available finite-element packages with respect to the CPU time and accuracy of the magnetic field.

Keywords: electromagnetic field analysis, accelerator magnets, magnetic moment method, magnetic surface charge method, meshing

1. Introduction

Most of the accelerator magnets are designed by means of electromagnetic simulations employing three-dimensional finite element method. OPERA-3D (TOSCA) is one of the major software for modeling accelerator magnets [1), 2)]. The name TOSCA comes from two scalar potentials, namely, reduced potentials and total potentials. The method has the following advantages. (i) Because it is based on the two-scalar-potential formulation, the number of degrees of freedom is small, and the magnetostatic analysis is fast. (ii) Coils are modeled as Biot-Savart sources and do not have to be meshed; therefore, the mesh quality of the magnetic core can easily be controlled.

Another famous software to model accelerator magnets is RADIA [3)–5)], which is freely distributed as Mathematica's add-on by ESRF: the European Synchrotron. The method has the following advantages. (i) Because it is based on the Magnetic Moment Method (hereafter MMM [6),7)]), no air-mesh is required, and no special technique is required to emulate open boundaries. (ii) Because only the magnetic core is meshed, it is fast and "lightweight," namely the size of the data is small. One problem of the MMM, which is also stated on Radia's website [3)], is the meshing problem. Figures 1 show a C-shaped electromagnet subdivided into (a) parallelepiped mesh and (b) mesh parallel to flux lines. If the iron core is subdivided into parallelepiped mesh, as shown in Fig. 1 (a), it is known that an inaccurate magnetic field is obtained. To avoid it, the iron core must be meshed parallel to flux lines, as shown in Fig. 1 (b), however, flux-line distributions must be known before solving the problem.

In this paper, the MMM with the idea of the Magnetic Surface Charge method (hereafter MMM with MSC) is proposed that is free from the above-mentioned meshing problem. Unknown variables in the MMM with MSC are surface magnetic charges on each face of the elements, whereas unknown variables in the MMM are magnetic moment vectors in each element. The negative magnetic point charges are placed at the center of the gravity of the element to guarantee Gauss's law in each element whose magnitudes are equal to the surface integral of each surface charge. By doing so, the bent of the magnetic flux in each element can be reproduced more naturally than the conventional MMM, even with coarse mesh. Accelerator magnets, such as a C-shaped dipole and a quadrupole magnet, are analyzed, and it is shown that the proposed method outperforms currently available finite-element packages with respect to the CPU time and accuracy of the magnetic field.

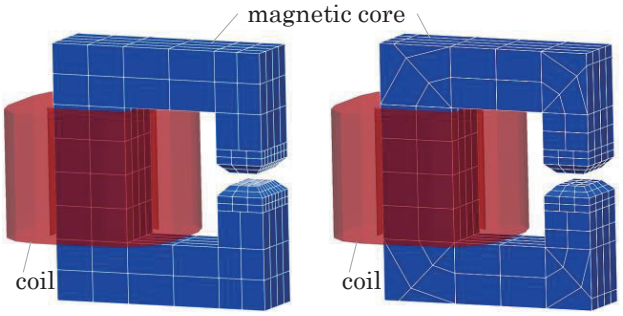

(a) parallelepiped mesh (b) parallel to flux lines

Fig. 1 Two different types of mesh for MMM.

2. Formulation

2-1. Conventional Magnetic Moment Method

A magnetic moment $\boldsymbol{M}$ in the element produces magnetic field $\boldsymbol{H}$ at observation point $\boldsymbol{r}$ by taking integrals as (1) where $\boldsymbol{r}'$, is the displacement $\boldsymbol{s}'$ is the surface, $\boldsymbol{V}'$, is the volume of the element, and $\boldsymbol{n}_{s'}$ is the normal vector of each surface[5)].

$$\boldsymbol{H}(\mathrm{r}) = \frac{1}{4\pi}\int \frac{(\boldsymbol{r}'-\boldsymbol{r})}{|\boldsymbol{r}'-\boldsymbol{r}|^3}\nabla\cdot\boldsymbol{M}dV' - \frac{1}{4\pi}\oint \frac{(\boldsymbol{r}'-\boldsymbol{r})}{|\boldsymbol{r}'-\boldsymbol{r}|^3}\boldsymbol{M}\cdot\boldsymbol{n}_{s'}dS' \tag{1}$$

Corresponding author: H. Yano
(e-mail: yano@elf.co.jp).

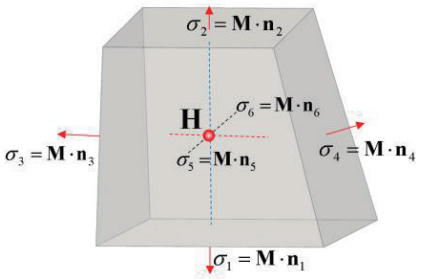

Fig. 2 Schematic of MMM's concept.

Figure 2 shows a schematic the concept of the MMM. Unknown variables in the MMM are magnetic moments $\boldsymbol{M}$ and thus the number of degrees of freedom is three per element. If $\boldsymbol{M}$ is assumed to be uniform inside the element, the first integral term in (1) vanishes; therefore, the matrix representation of the conventional MMM is derived from (2). The magnetic field produced by $\boldsymbol{M}$ is computed with the equivalent surface magnetic charges $\boldsymbol{M}\cdot\boldsymbol{n}_{s'}$. When the point matching method is employed, (2) is evaluated at the center of gravity of the element to construct a matrix equation.

$$\boldsymbol{H}(\boldsymbol{r}) = -\frac{1}{4\pi}\oint \frac{(\boldsymbol{r}'-\boldsymbol{r})}{|\boldsymbol{r}'-\boldsymbol{r}|^3}\boldsymbol{M}\cdot\boldsymbol{n}_{s'}dS' \qquad (2)$$

2-2. Magnetic Moment Method with the Idea of Surface Magnetic Charge Method

Figures 3 show schematic of the concept of the MMM with MSC. Hexahedral elements are subdivided into six pyramids and unknown variables are surface magnetic charge densities σ_n on each pyramid's bottom surface. Negative magnetic point charges m_n whose magnitudes are equal to the surface integral of the σ_n are placed at the vertex of each pyramid so that the total charges in each element are zeros in total. The number of degrees of freedom is six per element which is double the MMM. The magnetic fields H are evaluated at mid-points between the center of the surface and the center of gravity. The first integral term in (1) corresponds to the negative magnetic point charges and the second term to surface magnetic charges. The permeability is assumed to be constant, whereas the magnetic flux is not uniform and can bend in the element.

Figure 4 shows a simple two-dimensional magnetostatic problem. Two permanent magnets with the remanence of 0.2 T are attached to two adjacent edges of the iron core whose relative permeability is

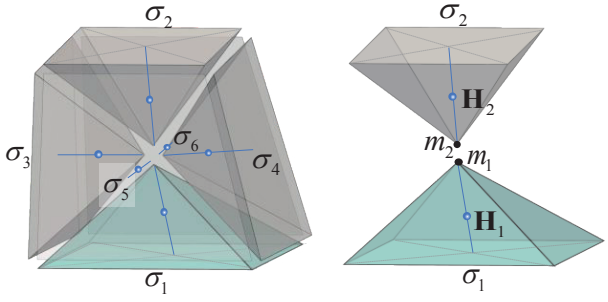

Fig. 3 Schematic of MMM with MSC's concept.

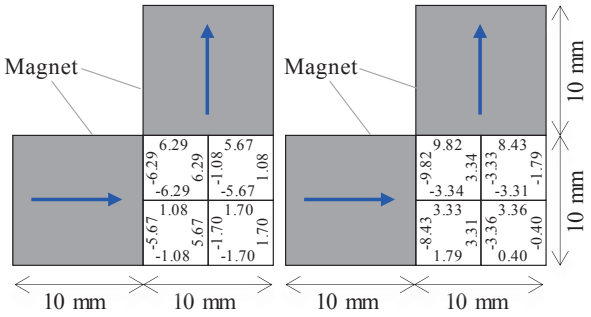

(a) MMM (b) MMM with MSC

Fig. 4 Simple two-dimensional static problem indicating the existence of the theoretical limit that can be achieved by the MMM.

1000. The iron core is subdivided into four squares. The obtained equivalent surface magnetic charge densities σ [Wb/m²] are shown in Fig. 4. If the permeability is uniform in the iron core, the equivalent magnetic charge densities on the inner surfaces of two adjacent elements must theoretically be zero in total. For example, in the MMM, at the bottom edge of the upper left square, σ = -6.29 Wb/m², and at the top edge of the lower left square, σ = 1.08 Wb/m², thus, they do not cancel each other. In the MMM with MSC, at the bottom edge of the upper left square σ = -3.34 Wb/m², and at the top edge of the lower left square, σ = 3.33 Wb/m², they are almost zero in total. This indicates that there is a theoretical limit to the accuracy that can be achieved with the MMM whereas the MMM with MSC is free from it.

3. Numerical results

3-1. T-Shaped magnet

Figures 5 show the T-shaped magnet; a typical example of which the MMM becomes inaccurate. A cuboid magnet is attached to a T-shaped magnetic core. The relative permeability of the magnetic core is 1000. and composed of four cubes with an edge length of 1 mm. The size of the permanent magnet is 1 mm × 1 mm × 2 mm and the and its remanence is 0.2 T The surface magnetic field distributions obtained by the MMM and the MMM with MSC are shown in Fig. 5. Upper figures are when the subdivision number N = 1 and lower figures are with N = 3. The result obtained by FEM with the 5 million mesh is used as the reference solution. Figure 6 shows the convergence of the surface magnetic field at the observation point P in increasing N. Even with N = 3, accurate results within sub-percent error can be obtained by MMM with MSC whereas the convergence of the MMM is slow and not simply monotonic.

3-2. C-Shaped magnet

A C-shaped magnet is a typical accelerator magnet, and an example model of RADIA is provided by ESRF[3]. Figures 7 show the three types of mesh of the C-shaped magnet: (a) parallelepiped coarse mesh, (b) parallelepiped fine mesh, and (c) mesh along flux lines.

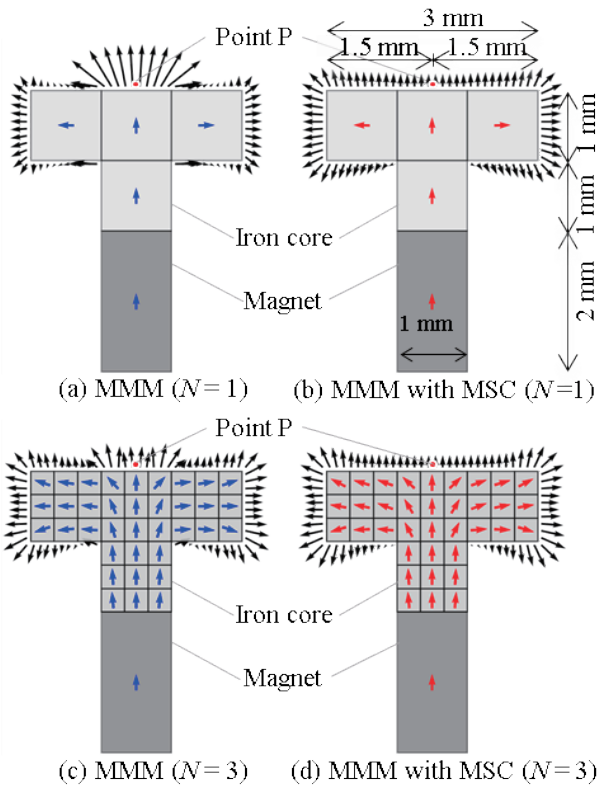

Fig. 5 T-shaped magnet example.

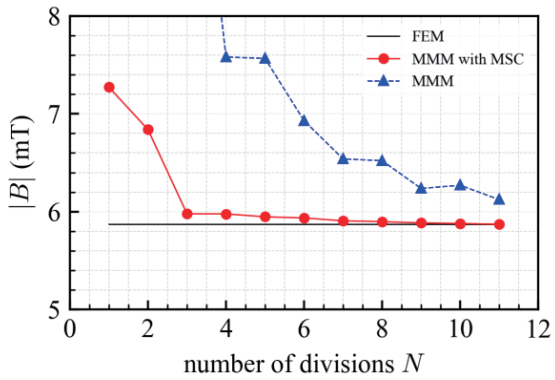

Fig. 6 Surface magnetic field at the point P.

The B-H curve of the magnetic core is shown in Figure 8.

The size of the magnetic core is 182.5 mm × 210 mm. The iron core gap is 10 mm and the magnetic field at the gap center is evaluated with various coil currents from 1000 to 10000 AT. The result obtained by OPERA-3D is used as the reference solution. 8-layer IABC [8), 9)] was required to obtain a self-consistent open boundary solution in OPERA-3D. Figures 9 show the magnetic field at the center of the gap and those errors with three types of mesh. Even with mesh type (a), the error of the magnetic field obtained by the MMM with MSC is about 4% at maximum. Both with mesh type (b) and (c), the error of the magnetic field obtained by the MMM with MSC is within sub percent, which indicates that the MMM with MSC is free from the meshing problem discussed in the introduction. The computing time for analyzing the C-shaped magnet with Intel Core i7-9700K CPU at 3.60 GHz is shown in Table 1. Although the computing time for the MMM is shorter than the MMM with MSC when the number of elements is the same, the results obtained by the MMM with MSC is more accurate especially when the mesh is coarse.

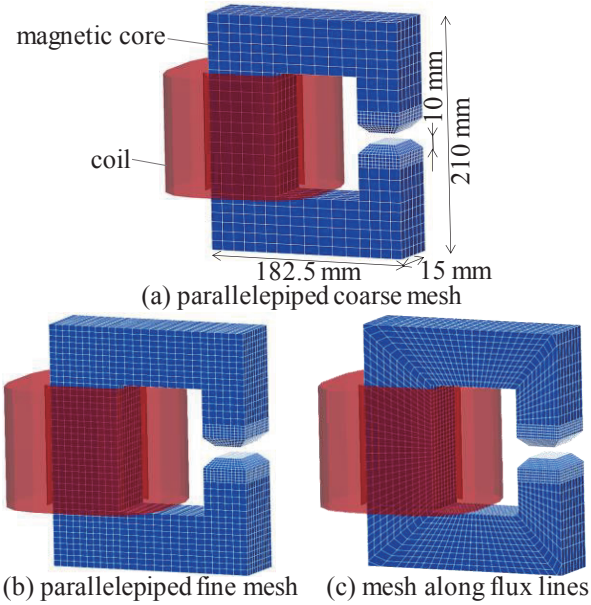

Fig. 7 Various mesh types of the C-shaped magnet.

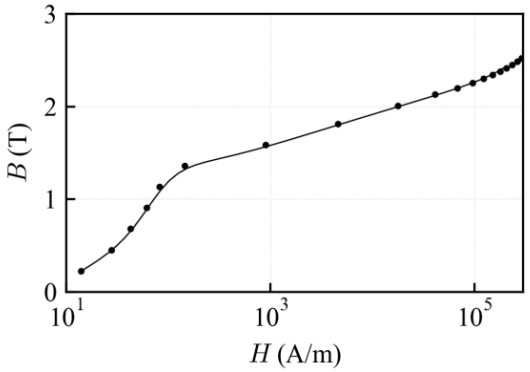

Fig. 8 B-H curve of the iron core.

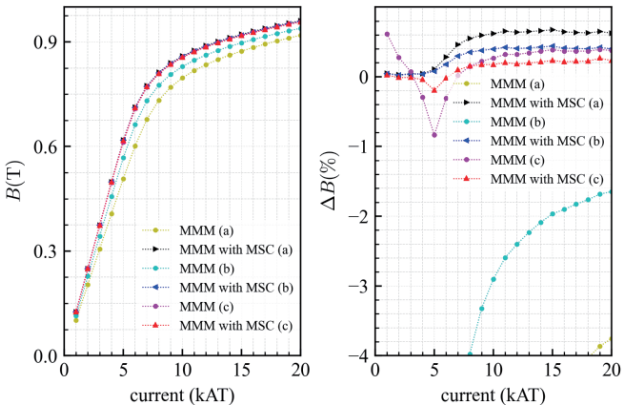

Fig. 9 Magnetic field and its errors at the gap center.

Table 1 CPU time for analysis of C-shaped magnet.

elements		method	current (AT)	CPU time (sec) mesh	solver
16,009,450		Opera3D	1000	6506	1885
			20000	6506	12231
(a)	1,200	MMM	1000	< 1	4
			20000	< 1	13
		MMM with MSC	1000	< 1	49
			20000	< 1	64
(b)	3,150	MMM	1000	1.2	29
			20000	1.2	152
		MM with MSC	1000	1.2	919
			20000	1.2	986
(c)	4,008	MMM	1000	1.5	55
			20000	1.5	261
		MMM with MSC	1000	1.5	1955
			20000	1.5	5428

3-3. Quadrupole magnet

A quadrupole magnet is also a typical accelerator magnet, and an example model of RADIA is provided by ESRF[3]. Figures 10 show the mesh of the quadrupole magnet. The size of the magnetic core is 176 mm × 176 mm. The B-H curve of the magnetic core is again shown in Fig. 8. Since the magnetic field at the center gap is zero in a quadrupole magnet, magnetic field at the Bohr radius is evaluated with various coil current densities from 0.5 to 5.0 mega ampere per square meter. The error of the magnetic field obtained by the MMM with MSC is within sub percent as shown in Figures 11. The computing time for analyzing the quadrupole magnet with Intel Core i7-9700K CPU at 3.60 GHz is shown in Table 2.

Table 2 CPU time for analysis of quadrupole magnet.

elements		method	current density (MA/m^2)	CPU time (sec) mesh	solver
9,013,890		Opera3D	0.5	2189	1623
			10.0	2189	24549
(a)	1,008	MMM	0.5	< 1	5
			10.0	< 1	12
		MMM with MSC	0.5	< 1	36
			10.0	< 1	45
(b)	640	MMM	0.5	< 1	3
			10.0	< 1	4
		MMM with MSC	0.5	< 1	10
			10.0	< 1	10

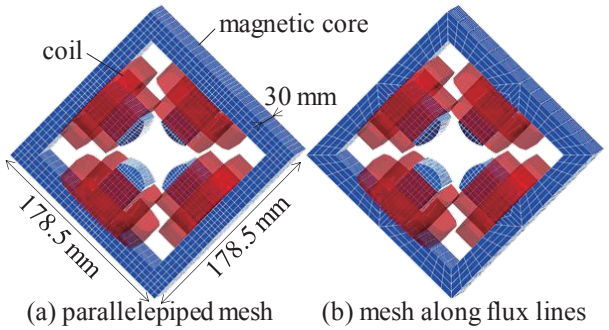

Fig. 10 Two different types of the mesh of the quadrupole magnet.

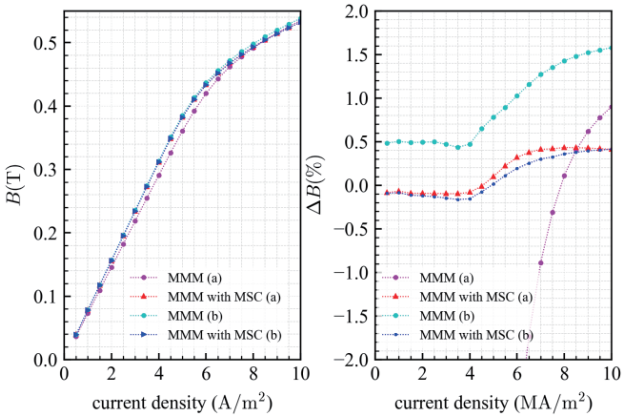

Fig. 11 Magnetic field and its errors at Bohr radius.

4. Conclusion

The Magnetic Moment Method with the idea of the Magnetic Surface Charge method is proposed that is free from the meshing problem. Unknown variables are surface magnetic charges on each face of the elements and the negative magnetic point charges are placed at the center of the gravity of the element. Accelerator magnets are analyzed, and it is shown that the proposed method outperforms currently available finite-element packages with respect to the CPU time and accuracy of the magnetic field. The proposed method is implemented in the commercial software ELF/MAGIC [10].

Acknowledgments This work was supported in part by the Japan Society for the Promotion of Science under Grants-in-Aid for Scientific Research (C) JP 20K04454.

References

1) Opera website: https://www.3ds.com/products-services/simulia/products/opera/ (As of Jan. 24, 2023).
2) J. Simkin and C. W. Trowbridge: *IEE Proc., Part B, Electric power applications.*, **127**, 368 (1980).
3) Radia website: https://www.esrf.eu/Accelerators/Groups/InsertionDevices/Software/Radia/ (As of Jan. 24, 2023).
4) O. Chadebec, J. L. Coulomb, and F. Janet: *IEEE Trans. Magn.*, **42**, 515 (2006).
5) O. Chubar, P. Elleaume, and J. Chavanne: *Journal of synchrotron radiation.*, **5**, 481 (1998).
6) F. Janet, J. L. Coulomb, C. Chillet, and P. Mas: *IEEE Trans. Magn.*, **41**, 1428 (2005).

7) T. Le Duc, O. Chadebec, J. M. Guichon, G. Meunier, and Y. Lembeey: *COMPEL - The international journal for computation and mathematics in electrical and electronic engineering.*, **32**, 333 (2012).
8) D. Meeker: *IEEE Trans. Magn.*, **49**, 5243 (2013).
9) K. Sugahara: *IEEE Trans. Magn.*, **53**, 7205604 (2017).
10) ELF/MAGIC website: https://www.elf.co.jp, (As of Jan. 24, 2023).

Received Nov. 16, 2022; Revised Dec. 16, 2022; Accepted Jan. 22, 2023

Editorial Committee Members・Paper Committee Members

Notice for Photocopying

編集委員・論文委員

複写をされる方へ

Journal of the Magnetics Society of Japan

Vol. 47 No. 2 (通巻第326号) 2023年3月1日発行

Vol. 47 No. 2 Published Mar. 1, 2023
by the Magnetics Society of Japan
Tokyo YWCA building Rm207, 1–8–11 Kanda surugadai, Chiyoda-ku, Tokyo 101–0062
Tel. +81–3–5281–0106 Fax. +81–3–5281–0107

Printed by JP Corporation Co., Ltd.
Sports Plaza building 401, 2–4–3, Shinkamata Ota-ku, Tokyo 144–0054
Advertising agency: Kagaku Gijutsu-sha

発行：(公社)日本磁気学会 101–0062 東京都千代田区神田駿河台 1–8–11 東京YWCA会館 207 号室
製作：ジェイピーシー 144–0054 東京都大田区新蒲田 2–4–3 スポーツプラザビル401 Tel.（03）6715–7915
広告取扱い：科学技術社 111–0052 東京都台東区柳橋 2–10–8 武田ビル 4F Tel.（03）5809–1132